

MATRIS: TOWARD RELIABLE AND EFFICIENT PRE-TRAINED MACHINE LEARNING INTERATOMIC POTENTIALS

Yuanchang Zhou^{1,2} Siyu Hu^{1,2} Xiangyu Zhang^{1,2} Hongyu Wang^{1,2,3}
Guangming Tan^{1,2} * Weile Jia^{1,2,*}

¹State Key Lab of Processors, Institute of Computing Technology, Chinese Academy of Sciences

²University of Chinese Academy of Sciences

³School of Advanced Interdisciplinary Sciences, UCAS

{zhouyuanchang23s, jiaweile}@ict.ac.cn

ABSTRACT

Foundation MLIPs demonstrate broad applicability across diverse material systems and have emerged as a powerful and transformative paradigm in chemical and computational materials science. Equivariant MLIPs achieve state-of-the-art accuracy in a wide range of benchmarks by incorporating equivariant inductive bias. However, the reliance on tensor products and high-degree representations makes them computationally costly. This raises a fundamental question: as quantum mechanical-based datasets continue to expand, can we develop a more compact model to thoroughly exploit high-dimensional atomic interactions? In this work, we present MatRIS (**M**aterials **R**epresentation and **I**nteraction **S**imulation), an invariant MLIP that introduces attention-based modeling of three-body interactions. MatRIS leverages a novel separable attention mechanism with linear complexity $O(N)$, enabling both scalability and expressiveness. MatRIS delivers accuracy comparable to that of leading equivariant models on a wide range of popular benchmarks (Matbench-Discovery, MatPES, MDR phonon, Molecular dataset, etc). Taking Matbench-Discovery as an example, MatRIS achieves an F1 score of up to 0.847 and attains comparable accuracy at a lower training cost. The work indicates that our carefully designed invariant models can match or exceed the accuracy of equivariant models at a fraction of the cost, shedding light on the development of accurate and efficient MLIPs.

1 INTRODUCTION

Quantum Mechanics (QM)-based calculations are the cornerstone of modern drug and material research, providing highly accurate modeling of interatomic interactions. However, their prohibitive computational cost makes large-scale simulations intractable (De Vivo et al., 2016; Jain et al., 2013b; Merchant et al., 2023). Machine learning interatomic potentials (MLIPs) have emerged as a powerful alternative, enabling accelerated, long-timescale molecular dynamics (MD) simulations while retaining near-quantum-chemical accuracy. With the increase in QM-based reference data and model innovations, MLIPs have demonstrated remarkable accuracy and generalization in property prediction and materials discovery (Merchant et al., 2023; Barroso-Luque et al., 2024; Zhang et al., 2024; Yang et al., 2024; Zhang et al., 2025; Fu et al., 2025; Wood et al., 2025).

Graph neural networks (GNNs) have been widely adopted for 3D molecular modeling, where atoms are represented as nodes and interatomic interactions as edges (Qu & Krishnapriyan, 2024; Liao & Smidt, 2023; Liao et al., 2024b; Fu et al., 2025). Through Message Passing (MP), node features are iteratively updated to capture local and global structural interactions. To enhance model expressiveness and generalization, many MLIPs incorporate domain-specific inductive biases (e.g., translation,

*Corresponding author

rotation, permutation, reflection invariance, or equivariance). Depending on how these symmetries are encoded, MLIPs are broadly divided into invariant, equivariant and unconstrained architectures (Duval et al., 2024; Jacobs et al., 2025). In invariant models, the structural descriptor is encoded based on attributes such as interatomic distances, bond angles, and dihedral angles (Gasteiger et al., 2020; 2022b; Klicpera et al., 2021; Deng et al., 2023; Zhang et al., 2025). In equivariant models, higher-order equivariance is typically enforced through computationally intensive tensor products of rotation order L (Batzner et al., 2022; Batatia et al., 2022; Liao & Smidt, 2023; Liao et al., 2024b). Previous work demonstrates that equivariant models often deliver superior accuracy (Batzner et al., 2022). In contrast, unconstrained models do not explicitly encode symmetries; instead, the model learns them from data or approximates them through data augmentation or auxiliary losses, leading to more flexible architectural design (Duval et al., 2024; Neumann et al., 2024; Rhodes et al., 2025). Meanwhile, the results in a popular benchmark (Matbench-Discovery leaderboard (Riebesell et al., 2025)) indicate that equivariant GNNs achieve higher accuracy. When the training data is MPTrj (Deng et al., 2023), eSEN-30M-MP (Fu et al., 2025) and eqV2 S DeNS (Barroso-Luque et al., 2024) reach F1 scores of 0.831 and 0.815, with energy errors of 0.033 and 0.036 meV/atom, respectively. Despite the accuracy gains, the heavy equivariant operations make equivariant methods significantly more computationally expensive and memory-intensive. Our investigation into the training cost of several mainstream pretrained models is summarized in Figure 1. eSEN-30M-MP and eqV2 S DeNS show superior F1 score while requiring 335 and 228 GPU days, respectively. This high computational demand can be caused by three main factors: 1) the intensive equivariant operations such as tensor products, 2) the large number of model parameters, and 3) the prolonged training schedules (e.g., 100, 150, and 600 training epochs are reported for eSEN-30M-MP, eqV2 S DeNS, and SevenNet-13i5 (Kim et al., 2025), respectively).

Incorporating equivariance into the GNN MLIPs serves as an implicit form of data augmentation. AlphaFold has shown that, with sufficient data, non-equivariant models can accurately predict protein secondary structures (Jumper et al., 2021; Abramson et al., 2024). In MLIPs, the rapid increase in QM-based reference datasets (Barroso-Luque et al., 2024; Levine et al., 2025; Gharakhanyan et al., 2025; Sriram et al., 2025) motivates us to ask: **Is the equivariance indispensable as the QM-based dataset continues to increase? Can we develop a more compact architecture to capture the high-dimensional atomic interactions encoded in QM-based data sufficiently?**

We have the following findings: 1) Recent studies (Yang et al., 2024; Zhang et al., 2024; 2025) show that invariant models offer reliable property predictions and enable a wide range of scientific applications while maintaining computational efficiency. 2) For a more compact architecture (i.e., one that can fully exploit QM-based data). Element types and pairwise interactions have been shown to be insufficient for distinguishing graphs with different chemical properties (Xu et al., 2019). Incorporating three-body interactions is needed to exploit the knowledge in QM-based data. Self-attention mechanisms (Mazitov et al., 2025; Qu & Krishnapriyan, 2024) have proven to be a promising method in improving model expressiveness, also benefiting in model scalability.

Building on these insights, we introduce an invariant MLIP: interatomic potential for **Materials Representation and Interaction Simulation (MatRIS)**. To the best of our knowledge, our model is the first to explicitly leverage an $O(N)$ attention mechanism to model three-body interactions. MatRIS consists of graph generation, feature embedding, graph attention, refinement, and a readout block. We provide the ablation study of these modules in this paper. Putting all these modules together, MatRIS achieves state-of-the-art (SOTA) accuracy and efficiency across a wide range of

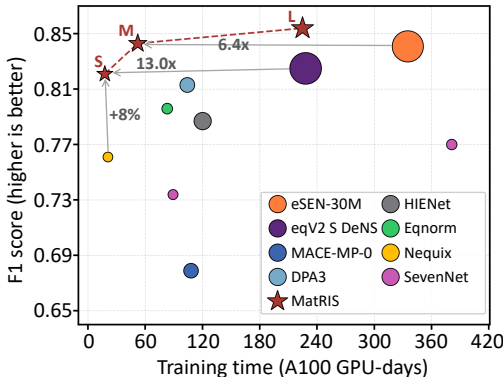


Figure 1: Trade-offs between training time and F1 score of foundation MLIPs. Training times for eSEN and eqV2 are estimated on Nvidia-A100. Nequix (Koker & Smidt, 2025) was trained on JAX; all others on PyTorch. Larger marks indicate models with more parameters.

chemical applications. Additionally, the novel separable attention has lower complexity ($O(N)$) compared to full attention ($O(N^2)$). Across diverse benchmarks, MatRIS achieves competitive results. MatRIS-L achieves SOTA results on compliant Matbench-Discovery with an F1 of **0.847** and a root mean square displacement (RMSD) of **0.0717**. Moreover, MatRIS-S and MatRIS-M deliver accuracy comparable to eqV2 S DeNS and eSEN-30M-MP, respectively, while improving training efficiency by **13.0** \times and **6.4** \times , respectively. These results demonstrate MatRIS’s strong potential for applications in materials science and drug discovery.

2 RELATED WORKS

Invariant MLIPs. Invariant MLIPs are models whose intermediate representations are invariant under rotations and translations (Duval et al., 2024). This invariance is achieved by using internal coordinates instead of Cartesian coordinates, with features such as interatomic distances, bond angles, and dihedral angles remaining unchanged under rotations and translations of the system (Schütt et al., 2017; Gasteiger et al., 2020; Novikov et al., 2020; Fan et al., 2022; Gasteiger et al., 2022b; Chen & Ong, 2022; Deng et al., 2023; Zhang et al., 2025). Early invariant MLIPs, such as SchNet (Schütt et al., 2017), CGCNN (Xie & Grossman, 2018), and PhysNet (Unke & Meuwly, 2019), employ relative distances between node pairs and encode local geometric information via learnable radial basis functions. More recent MLIPs enhance representational expressiveness by incorporating higher-order many-body scalar features. For example, the DimeNet (Gasteiger et al., 2020; 2022a) series introduced directional message passing, allowing angular information to be embedded in edge updates between atoms. The GemNet series (Gasteiger et al., 2022b; Klicpera et al., 2021) further incorporates dihedral angles to improve performance. SphereNet (Liu et al., 2022) and ComENet (Wang et al., 2022) proposed methods to efficiently extract four-body angles within local neighborhoods, avoiding the need to iterate over all three-hop neighbors. DPA3 (Zhang et al., 2025) builds upon the line graph series (LiGS), capturing higher-order interactions. Invariant MLIPs are progressively increasing their representational expressiveness while maintaining inherent computational efficiency. Building upon these insights, we design MatRIS from an invariant perspective. We further provide a detailed discussion in Appendix A, highlighting how MatRIS differs from other MLIPs that incorporate three-body encodings or attention-based mechanisms.

Equivariant MLIPs. Equivariant MLIPs are models where intermediate representations are invariant (e.g., scalars) or equivariant (e.g., vectors or higher-order tensors) under rotations (Duval et al., 2024). Current equivariant MLIPs can be divided into scalarization-based models (Schütt et al., 2021; Du et al., 2023; Thölke & Fabritiis, 2022; Aykent & Xia, 2025) and high-degree steerable models (Musaelian et al., 2023; Batzner et al., 2022; Batatia et al., 2022; Liao & Smidt, 2023). Scalarization-based MLIPs model interatomic interactions in the Cartesian coordinate system while restricting the set of operations on geometric features to preserve equivariance (Duval et al., 2024; Wang et al., 2024; Yin et al., 2025). On the other hand, high-degree steerable equivariant MLIPs use irreducible representations (irreps) to encode features, ensuring equivariance under 3D rotations. Each irrep of degree L corresponds to a $(2L + 1)$ -dimensional vector space (Batzner et al., 2022; Batatia et al., 2022; Liao & Smidt, 2023). In equivariant GNN-based MLIPs, MP involves transforming and combining these type- L vectors. To interact across degrees during MP, tensor products (by using Clebsch–Gordan coefficients to combine) are employed. To avoid excessive computational complexity, these models typically employ only low-degree equivariant representations (Park et al., 2024; Liao et al., 2024b; Fu et al., 2025). Equivariant MLIPs continue to deliver SOTA accuracy on various benchmarks (Tran et al., 2023; Riebesell et al., 2025), while remaining computationally demanding.

Unconstrained MLIPs. Unconstrained MLIPs do not impose strict constraints on their intermediate representations. Instead, these models typically learn symmetries directly from the data or incorporate additional loss terms to encourage symmetry learning (Duval et al., 2024; Rhodes et al., 2025). For example, Qu & Krishnapriyan (2024); Neumann et al. (2024); Rhodes et al. (2025) use data augmentation (applying random rotations to training samples) to learn rotational equivariance and have demonstrated promising results. In addition, Neumann et al. (2024) enhances stability in MD simulations by removing net force and torque, while Rhodes et al. (2025) introduces an ‘Equigrad’ loss to incentivize rotational invariance of energy. Unconstrained MLIPs have inference efficiency comparable to invariant MLIPs and more flexible architectures. These models

demonstrate competitive accuracy in multiple benchmarks (Chanussot et al., 2021; Tran et al., 2023; Riebesell et al., 2025). However, studies indicate that they may lead to errors in certain property prediction tasks (Fu et al., 2023; Póta et al., 2025; Bigi et al., 2025).

3 MATRIS

In this section, we introduce the detailed architecture of MatRIS. The interaction between the atom graph and the line graph is described in Section 3.1. The Graph Attention module is depicted in Section 3.2. In Section 3.3, we describe other key components of MatRIS. An overview of MatRIS is shown in Figure 3, and the model formalizations are detailed in Appendix B.

3.1 LINE-ATOM GRAPH INTERACTION

To model three-body interactions, we explicitly construct a Line Graph. In the Atom Graph, nodes represent atom types and edges represent pairwise interactions (bonds), whereas in the Line Graph, nodes represent edges of the atom graph and edges represent three-body interactions (angles) (Harary & Norman, 1960; Whitney, 1992).

Specifically, given an Atom Graph $G^a = (V^a, E^a)$, where V^a is the set of atoms and E^a is the set of edges within a cutoff distance r_{cut}^a , the corresponding Line Graph $G^l = (V^l, E^l)$ is constructed as follows: ① Each node in V^l corresponds to an edge in E^a ; ② An edge $e \in E^l$ is added between two nodes if their corresponding edges in E^a share a common atom, representing the angular information formed by the three atoms (i.e., the three-body interaction). The conversion from the atom graph to the line graph is illustrated in Figure 2.

For graph information fusion, we update the Line Graph to obtain edge and angular features that encode three-body interactions. These updated edge features are then propagated back to the Atom Graph, enabling the atomic features to incorporate higher-order information from the Line Graph.

3.2 GRAPH ATTENTION

In this section, we introduce the design motivation and implementation of the Dim-wise Softmax and Separable Attention mechanisms.

Dim-wise Softmax. Recent studies have shown that attention mechanisms play an important role in improving both the accuracy and scalability of MLIPs (Liao & Smidt, 2023; Liao et al., 2024b; Qu & Krishnapriyan, 2024). Existing approaches (Liao & Smidt, 2023; Wang et al., 2024; Shao et al., 2025; Liao et al., 2024b) typically compute attention weights a_{id} to weight the value vectors $V \in \mathbb{R}^{\text{neighbors} \times D}$, where D denotes the hidden dimension. The weights a_{id} depend on the features of node i and its neighbors $\mathcal{N}(i)$, while the values V are obtained by applying a nonlinear transformation to the fused edge and node features.

In these methods, the same attention weights are applied to all feature dimensions, implicitly assuming equal importance across dimensions. However, this assumption limits the model’s ability to distinguish the independent contributions of different feature dimensions. Our proposed Dim-wise Softmax computes attention scores independently for each feature dimension. Given an input feature $x \in \mathbb{R}^{\text{neighbors} \times D}$ and a neighbor list \mathcal{N} , the Dim-wise Softmax is computed as follows:

$$\alpha_{id} = \text{Dim-wise Softmax}(x_{id}, \mathcal{N}(i)) = \frac{\exp(x_{id})}{\sum_{k \in \mathcal{N}(i)} \exp(x_{kd})} \quad (1)$$

where $\alpha \in \mathbb{R}^{\text{neighbors} \times D}$ is the attention weight matrix, x_{id} denotes the d -th feature of node i , and $\mathcal{N}(i)$ represents the set of neighboring nodes of node i . This approach preserves the independence

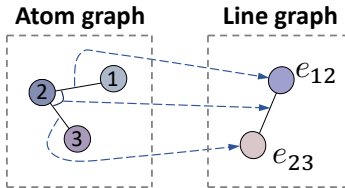


Figure 2: Conversion from an Atom Graph to a Line Graph.

of feature dimensions while emphasizing the relative importance of different neighbors in each dimension, thereby enhancing the model’s ability to capture local structural information.

Separable Attention. In molecular systems, interatomic interactions are directional, and each atom plays two roles: target node and source node. Most existing methods only aggregate information from the source node to the target node (Liao & Smidt, 2023; Liao et al., 2024b; Wang et al., 2024; Shao et al., 2025), which assumes symmetric information flow. However, this is not always true in real physical systems. For example, in polar bonds, charged environments, or local defect structures, the effect of the source node on the target node can differ from the effect of the target node on the source node (Bengtsson, 1999; Kühne & Khaliullin, 2013). To address this, we introduce two independent sets of attention weights: source attention weights and target attention weights. The first models how neighboring nodes affect the central node, while the second captures how the central node influences its neighbors. In this way, the two roles of nodes are explicitly separated during aggregation. The overall workflow is illustrated in Figure 3(b). Given the interaction e_{ij} between a target node v_i and a source node v_j , we compute the attention weights as follows:

$$t_{ij} = \text{Linear}(e_{ij}) \quad \text{and} \quad ta_{ij} = \text{Dim-wise Softmax}(t_{ij}, \mathcal{N}(i)) \quad (2)$$

$$s_{ij} = \text{Linear}(e_{ij}) \quad \text{and} \quad sa_{ij} = \text{Dim-wise Softmax}(s_{ij}, \mathcal{N}(j)) \quad (3)$$

Here, $\mathcal{N}(i)$ and $\mathcal{N}(j)$ denote the indices of the target and source nodes, respectively. The final attention outputs are obtained as the weighted sum of ta_{ij} , sa_{ij} , and e'_{ij} . Here, e'_{ij} is obtained by concatenating e_{ij} , v_i , and v_j , followed by target and source feature fusion through a gMLP (see Figure 3(d)). The two attention branches share the same computational flow and can therefore be executed in parallel. We also implement optimized kernels to improve training efficiency.

Generality Analysis. As mentioned earlier, many MLIPs are either unconstrained or equivariant. Unconstrained MLIPs are flexible, allowing Dim-wise Softmax and Separable Attention to be applied directly. For equivariant MLIPs, symmetry must be preserved. To ensure this, Dim-wise Softmax is computed on invariant features (e.g., $L = 0$), producing attention weights that are invariant. These weights are then applied to equivariant features within each irrep channel, without mixing components of different orders, ensuring the features remain equivariant under geometric transformations. Separable Attention extends this approach with two branches, computing attention equivariantly and aggregating information separately over the indices of the target and source nodes.

3.3 OVERALL ARCHITECTURE

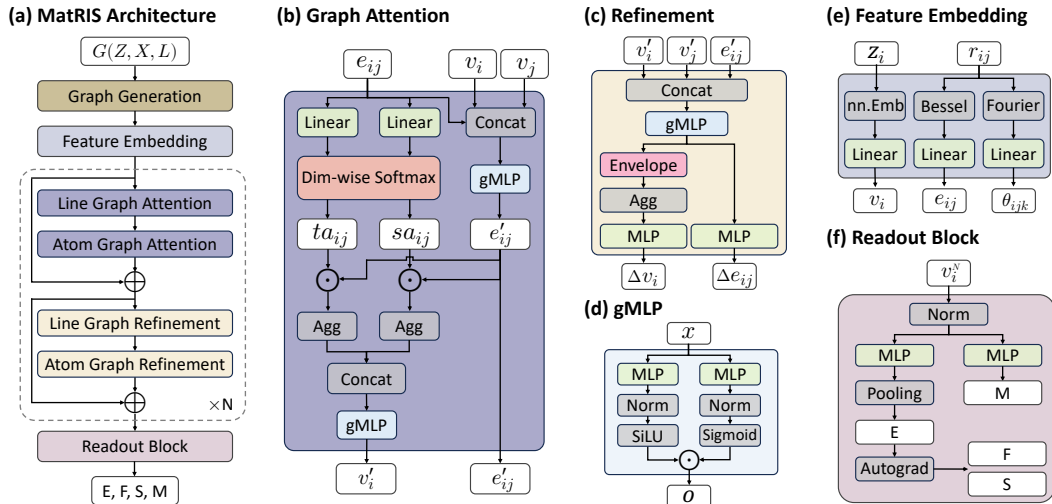


Figure 3: Overview of MatRIS. The model architecture (a) consists of feature embedding (e), graph attention (b), refinement (c), and a readout block(f).

Graph Generation. Given a crystalline system $G(Z, X, L)$, where $Z \in \mathbb{R}^{\text{natoms}}$ denotes the atomic numbers, $X \in \mathbb{R}^{\text{natoms} \times 3}$ represents the atomic coordinates, and $L \in \mathbb{R}^{3 \times 3}$ refers to the lattice. We first perform periodic repetition of the structure and then employ a radius-cutoff graph construction to represent it. Inspired by CHGNet (Deng et al., 2023), we construct the atom graph G^a (with atoms as nodes and bonds as edges) based on r_{cut}^a and the line graph G^l (with bonds as nodes and angles as edges) based on r_{cut}^l for the crystal structure.

Feature Embedding. Atomic numbers are initialized using trainable embeddings, while pairwise distances are encoded via a learnable radial Bessel basis with envelope functions (Gasteiger et al., 2020). For bond angles, we employ a learnable Fourier basis expansion following Deng et al. (2023). These input features are then passed through a linear layer to generate initial node, edge, and three-body representations. This block is illustrated in Figure 3(e).

Refinement. The output of Graph Attention v_i^l and e_{ij}^l is concatenated and processed by a gMLP operator (shown in Figure 3(c)). This representation is further refined by an Envelope function (Gasteiger et al., 2020) (ensures smoothness). The refined signals are then aggregated over neighboring interactions, enabling each edge to integrate local information. Finally, the output is transformed by a MLP operator to produce the residual node features Δv_i and edge features Δe_{ij} .

Readout Block. The Readout Block (Figure 3(f)) takes node features v_i from the last layer. After the normalization layer, the features are passed through MLPs to predict atomic energies and magnetic moments (M). Atomic energies are summed to obtain total energy (E). To ensure the reliability (Bigi et al., 2025), forces (F_i) and stress (σ) are computed by Equation 4. \mathcal{V} is volume.

$$F_i = -\frac{\partial E}{\partial X_i}, \sigma = \frac{1}{\mathcal{V}} \frac{\partial E}{\partial \epsilon} \quad (4)$$

4 EXPERIMENTS

We evaluated MatRIS on Matbench-Discovery benchmark (Section 4.1), MatPES benchmark (Section 4.2), MDR phonon benchmark (Section 4.3), Molecular zero-shot benchmark (Section 4.4). The best results are in bold, and the second best are underlined. Moreover, we conducted ablation studies on the network modules and training methods (Section 4.5). Finally, we analyzed the efficiency of MatRIS (Section 4.6). In addition, the results of experiments on the Matbench-Discovery benchmark (non-compliant), LAMBench benchmark (Peng et al., 2026), Zeolite benchmark (Yin et al., 2025), DPA2 test sets (Zhang et al., 2024) and MD stability evaluation are provided in Appendix D. The training strategies are introduced in Appendix C, and the training hyperparameter settings are detailed in Appendix E.

4.1 MATBENCH DISCOVERY

Dataset and Setting. The Matbench-Discovery benchmark (Riebesell et al., 2025) is a well-established benchmark for evaluating the ability of models in new material discovery. In this benchmark, all models are required to optimize the geometry and predict the formation energy of each of the 256k structures in the WBM test set (Wang et al., 2021). These results are then used to assess thermodynamic stability at the ground state (0 K). In the ‘‘compliant’’ setting, all models are required to use MPTrj (Deng et al., 2023) as the training dataset, whereas in the ‘‘non-compliant’’ setting, this requirement is relaxed (the results are reported in Appendix D.1). More details on the hyperparameters can be found in Table 12. Moreover, inspired by Zaidi et al. (2023) and Liao et al. (2024a), we apply denoising pretraining to MatRIS-M and MatRIS-L. The specific details are described in Appendix E. Notably, this denoising is also adopted in several other works (ORB v2 MPTrj (Neumann et al., 2024), eqV2 S DeNS, and eSEN-30M-MP). Structures are relaxed using MatRIS and the FIRE (Bitzek et al., 2006) optimizer, with convergence reached after 500 steps or when the maximum force falls below 0.05 eV/Å.

Results of the Compliant Benchmark We summarize the comparison with other models in Table 1. MatRIS-S/M achieves performance comparable to eqV2 S DeNS/eSEN-30M-MP while using fewer parameters and lower computational costs (see Figure 1 for a comparison of training cost).

Table 1: MatRIS performance on the compliant Matbench-Discovery benchmark with results on unique structure prototypes. ‘ \uparrow ’/‘ \downarrow ’ stands for higher/lower is better.

Model	Param.	F1 \uparrow	DAF \uparrow	Precision \uparrow	Recall \uparrow	Accuracy \uparrow	MAE \downarrow	R2 \uparrow	$K_{srme}\downarrow$	RMSD \downarrow
CHGNet	0.41M	0.613	3.361	0.514	0.758	0.851	0.063	0.689	1.717	0.0949
MACE-MP-0	4.69M	0.669	3.777	0.577	0.796	0.878	0.057	0.697	0.647	0.0915
GRACE-2L	15.3M	0.691	4.163	0.636	0.757	0.896	0.052	0.741	0.525	0.0897
Allegro-MP-L	18.7M	0.751	4.516	0.690	0.823	0.915	0.044	0.778	0.504	0.0816
Nequix MP	0.71M	0.751	4.455	0.681	0.836	0.914	0.044	0.782	0.446	0.0853
SevenNet-13i5	1.17M	0.760	4.629	0.708	0.821	0.920	0.044	0.776	0.550	0.0847
NequIP-MP-L	9.6M	0.761	4.704	0.719	0.809	0.921	0.043	0.791	0.452	0.0856
ORB v2 MPTrj	25.2M	0.765	4.702	0.719	0.817	0.922	0.045	0.756	1.725	0.1007
HIENet	7.51M	0.777	4.932	0.754	0.801	0.929	0.041	0.793	0.642	0.0795
Eqnorm MPTrj	1.31M	0.786	4.844	0.741	0.838	0.929	0.040	0.799	<u>0.408</u>	0.0837
DPA-3.1-MPTrj	4.81M	0.803	5.024	0.768	0.841	0.936	0.037	0.812	0.650	0.0801
eqV2 S DeNS	31.2M	0.815	5.042	0.771	<u>0.864</u>	0.941	0.036	0.788	1.676	0.0757
eSEN-30M-MP	30.1M	0.831	5.260	0.804	0.861	0.946	<u>0.033</u>	<u>0.822</u>	0.340	0.0752
MatRIS-S	4.3M	0.811	5.127	0.784	0.840	0.940	0.036	0.803	0.730	0.0766
MatRIS-M	6.3M	<u>0.833</u>	<u>5.363</u>	<u>0.820</u>	0.847	<u>0.948</u>	<u>0.033</u>	0.820	0.542	<u>0.0742</u>
MatRIS-L	10.4M	0.847	5.422	0.829	0.865	0.951	0.031	0.829	0.489	0.0717

These results demonstrate the effectiveness of MatRIS. Moreover, MatRIS-L achieves SOTA performance across all metrics, with an F1 score of 0.847. It also achieves an RMSD of 0.0717 when comparing relaxed structures to DFT reference values.

4.2 MATCALC BENCHMARK

Table 2: Summary of model performance on the MatCalc benchmark. All results were obtained using the MatCalc package and its associated dataset.

Model	Param.	Equilibrium		Near-equilibrium			
		$d\downarrow$	$Ef\downarrow$	$K\downarrow$	$G\downarrow$	$CV\downarrow$	$f/f_{DFT}\uparrow$
MatPES-trained models							
M3GNet	0.66M	<u>0.42</u>	0.11	26	25	27	0.97
CHGNet	2.7M	0.43	0.082	24	21	23	0.91
TensorNet	0.84M	0.37	<u>0.081</u>	<u>18</u>	<u>15</u>	13	0.93
MatRIS	1.4M	0.54	0.068	15	13	<u>16</u>	<u>0.96</u>
MPTrj-trained models							
CHGNet	2.7M	0.51	0.092	17.0	30.0	24.0	0.830
MACE-L	5.7M	0.43	–	25.3	<u>22.5</u>	11.6	0.829
SevenNet-13i5	1.17M	0.55	0.057	<u>13.2</u>	170.2	8.03	0.922
eqV2 S DeNS	31.2M	0.25	0.033	27.2	29.1	25.9	0.964
eSEN-30M-MP	30.1M	0.34	<u>0.039</u>	18.8	77.3	4.66	0.986
MatRIS-M	6.3M	<u>0.32</u>	0.041	12.4	16.4	<u>7.39</u>	<u>0.983</u>
OAM-trained models							
SevenNet-MF-ompa	25.7M	0.502	0.028	13.3	32.2	4.60	0.976
eqV2 M	86.6M	0.235	0.017	25.4	17.5	80.4	0.999
eSEN-30M-OAM	30.1M	<u>0.299</u>	0.089	11.9	14.8	<u>4.35</u>	<u>0.996</u>
MatRIS-10M-OAM	10.4M	0.316	<u>0.025</u>	10.6	13.3	3.97	0.985

Dataset and Settings. MatCalc benchmark (Kaplan et al., 2025) covers equilibrium properties (relaxed structure similarity d , formation energy Ef), near-equilibrium properties (bulk modulus K , shear modulus G , constant-volume heat capacity CV , force softening f/f_{DFT}), and is constructed from test data collected from the Materials Project (Jain et al., 2013a), Alexandria (Schmidt et al., 2024), WBM high-energy states (Wang et al., 2021). We compare models trained on MatPES-PBE (Kaplan et al., 2025), MPTrj and OAM, with the results reported in Table 2. We maintained consistent evaluation settings for all MPTrj- and OAM-trained models. Specifically, for elastic moduli calculations, we applied normal (diagonal) strain magnitudes of ± 0.01 and ± 0.005 for ϵ_{11} , ϵ_{22} , ϵ_{33} , and off-diagonal strain magnitudes of ± 0.06 and ± 0.03 for ϵ_{23} , ϵ_{13} , ϵ_{12} .

Results and Analysis. Table 2 summarizes the performance of models trained on the MatPES-PBE, MPTrj and OAM datasets. For models trained on MatPES-PBE, MatRIS achieves the best overall performance, clearly outperforming other models in predicting formation energy E_f .

For models trained on MPTrj, MatRIS attains SOTA or near-SOTA results on 83% of the evaluated metrics. Notably, MatRIS remains robust on “Near-equilibrium” tasks regardless of the training dataset. Although the higher fraction of near-equilibrium structures in MPTrj amplifies PES “Softening” (f/f_{DFT}) (Deng et al., 2024; Kaplan et al., 2025), MatRIS maintains stable performance. Comparisons with CHGNet further indicate that changing the training dataset does not result in significant softening, underscoring the effectiveness of the architectural design.

The same trend is observed for models trained on OAM, where MatRIS-10M-OAM performs robustly across all metrics and achieves SOTA performance overall.

4.3 MDR PHONON BENCHMARK

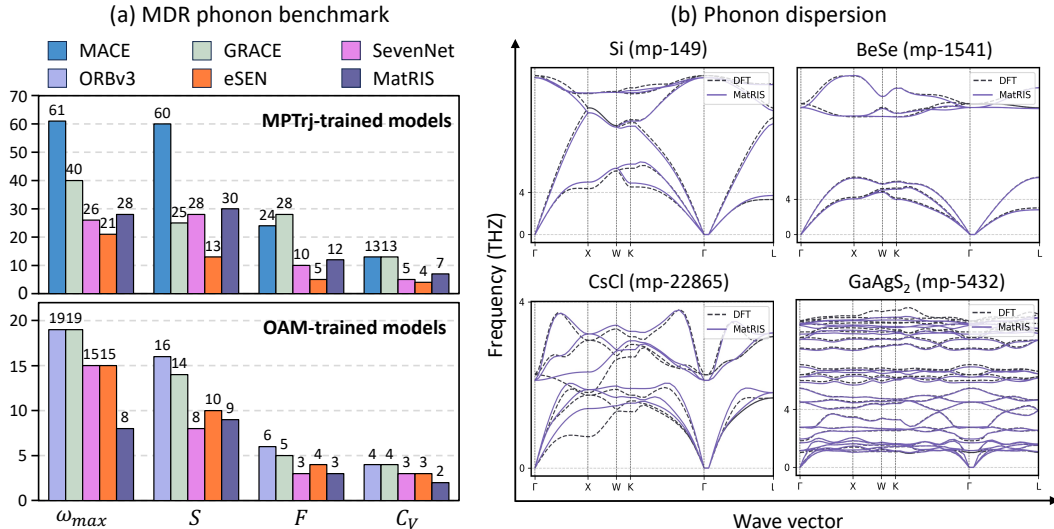


Figure 4: (a) Summary of model performance on the MDR phonon benchmark. The evaluation metrics include ω_{max} (K), S (J/K/mol), F (kJ/mol), and C_V (J/K/mol), where the reported values represent the MAE between the model predictions and the DFT results. (b) Predicted phonon dispersion obtained using MatRIS with a 0.01Å displacement. The DFT results are taken from the phononDB dataset.

Dataset and Settings. The MDR phonon benchmark (Loew et al., 2025) is used to evaluate the ability of MLIPs to predict phonon properties. It requires MLIPs to compute the maximum phonon frequency (ω_{max}), entropy (S), free energy (F), and heat capacity at constant volume (C_V) for approximately 10,000 structures. To ensure a fair comparison, we follow the evaluation protocol adopted in Loew et al. (2025). Specifically, we first optimize the structures using the FIRE optimizer (max steps=500, fmax=0.005). Displacements are generated with a magnitude of 0.01 Å, and the properties are computed at 300 K.

Results and Analysis. Results for both the MPTrj-trained and OAM-trained models are shown in Figure 4(a). MatRIS achieves competitive results among the MPTrj-trained models. As the training dataset grows, MatRIS-10M-OAM achieves SOTA accuracy on most metrics, with a particularly significant improvement in the maximum phonon frequency (ω_{max}). It is worth noting that MatRIS-10M-OAM achieves higher accuracy, with values of ω_{max} , S , F , and C_V being 7.08, 7.12, 2.12, and 1.91, respectively.

We also selected four representative structures from the phononDB dataset (Togo) for visualization, as shown in Figure 4(b). We find that MatRIS-MP-L not only reproduces the highest frequencies but also aligns well with the DFT results overall.

4.4 MOLECULAR ZERO-SHOT BENCHMARK

Table 3: MatRIS performance on the Molecular zero-shot benchmark. Energy (E) is reported in kcal/mol and Force (F) in kcal/mol/Å.

Model	TorsionNet-500				MD22 (Ac-Ala3-NHMe)		ANI-1x		AIMD-Chig	
	E MAE	E RMSE	MAEB ^a	NABH _h ^b	E	F	E	F	E	F
AIMNet2	0.38	0.55	0.58	82	–	–	–	–	–	–
DPA2-Drug	0.24	0.35	0.36	18	–	–	–	–	–	–
MACE-OFF-L	0.14	0.21	0.23	4	<u>2.29</u>	<u>5.205</u>	<u>5.82</u>	3.948	<u>8.25</u>	<u>3.853</u>
DPA3-L24	<u>0.06</u>	<u>0.09</u>	<u>0.09</u>	0	–	–	–	–	–	–
MatRIS-M	0.04	0.07	0.07	0	2.23	5.140	4.15	<u>4.414</u>	1.55	3.604

^a The MAE of the torsional barrier height is defined as the energy difference between the minimum and maximum along the torsional rotation.

^b The number of molecules with barrier height errors exceeding 1 kcal/mol.

Dataset and Settings. AIMNet and DPA2-Drug were trained on the datasets from Anstine et al. (2025) and Yang et al. (2025), respectively, while the other models were pre-trained on SPICE-MACE-OFF23 (Kovács et al., 2025), which contains 951,005 small-molecule configurations. The energies and forces of all configurations were computed at the ω B97M-D3(BJ)/def2-TZVPPD level. Following Peng et al. (2026), we selected the Ac-Ala3-NHMe from the MD22 (Chmiela et al., 2023), ANI-1x (Smith et al., 2018), and AIMD-Chig (Wang et al., 2023) datasets, which contain 2,212, 8,861, and 19,800 configurations, respectively. The training parameters can be found at Table 12 in appendix. For the MD22, ANI-1x, and AIMD-Chig benchmarks, we corrected inconsistencies caused by differences between DFT functionals.

Results and Analysis. We selected available molecular pre-trained models (MACE-OFF-L (Kovács et al., 2025) and DPA3-L24 for comparison, and the results are summarized in Table 3. MatRIS-M performs well across four downstream datasets. On the TorsionNet-500 test set, its energy prediction error is reduced by about 22.2%–33.3% compared to the current SOTA model DPA3. In the remaining three datasets, MatRIS-M ranks first in five out of six metrics and second in the remaining one, demonstrating that it effectively leverages the knowledge from the pre-training dataset to achieve more reliable performance on downstream tasks.

4.5 ABLATION STUDY

We conduct ablation studies on various modules of MatRIS and their corresponding training methods. We train the MatRIS-S on MPTrj and evaluate it on 15,000 randomly sampled structures from the WBM dataset, reporting performance using the MAE of formation energies.

Table 4: Ablation studies. Formation energy (**Ef**) MAE is in meV/atom, lower is better.

Index	Dim-wise softmax	Separable attention	Learnable envelope	Ef (MAE)	Index	Denoising pretraining	With magmom	Graph-level loss	Ef (MAE)
1	✓	✓	✓	28.0	1	✓	✓	✓	27.2
2	✗	✓	✓	28.4	2	✗	✓	✓	28.0
3	✗	✗	✓	29.1	3	✗	✗	✓	29.7
4	✗	✗	✗	31.3	4	✗	✗	✗	30.2

(a) Effect of modules: dim-wise softmax, separable attention and learnable envelope.

(b) Effect of training methods: denoising pretraining, magnetic moment prediction, and graph-level loss.

Module Ablation. We evaluated the impact of Dim-wise Softmax, Separable Attention, and Learnable Envelope on model accuracy, as shown in Table 4(a). Specifically, replacing Dim-wise Softmax with standard softmax (i.e., sharing the same weight across all feature dimensions) increased MAE to 28.4 meV/atom (Index 2). Subsequently, restricting attention-based aggregation to the source-to-target direction further increased MAE (Index 3). Finally, replacing the learnable envelope function with a fixed one also degraded performance (Index 4).

Training Method Ablation. We further analyze the contributions of different training strategies to model performance, as shown in Table 4(b). Pretraining with denoising (see Section C.3 in appendix) effectively improves performance, as predicting noise helps mitigate over-smoothing (Godwin et al., 2022; Zaidi et al., 2023). Notably, predicting magmoms also enhances accuracy, since magmoms help distinguish features in different chemical environments and, being a node-level task, likely reduce over-smoothing during training (Deng et al., 2023). Finally, performing loss reduction at the graph level prevents the force loss from being biased by differences in system size (see Section C.2 in appendix for more detail), further improving performance.

4.6 EFFICIENCY-ACCURACY ANALYSIS.

In this section, we compare the computational efficiency of MatRIS with several SOTA models (benchmarked without `torch.compile` or optimized kernels).

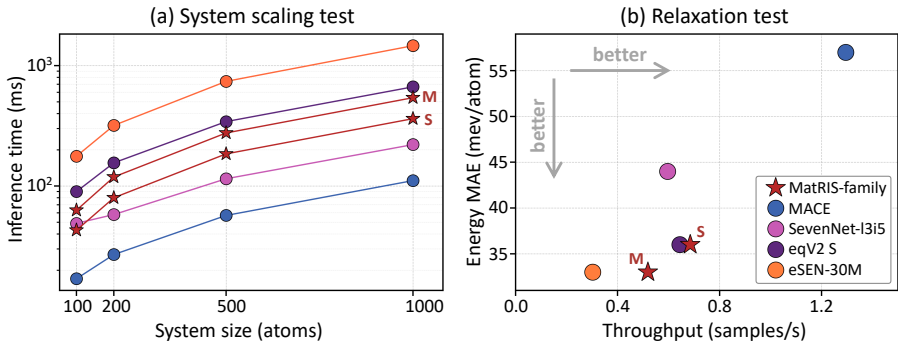


Figure 5: Efficiency-accuracy comparison.

The inference time across system sizes (excluding graph construction) is summarized in Figure 5(a). MatRIS demonstrates higher efficiency than eqV2 and eSEN but lower than MACE-L, as MACE-L utilizes only 2 layers while MatRIS-S and MatRIS-M employ 4 and 6 layers, respectively.

We further evaluate the models in practical applications. We randomly select 500 structures from the WBM dataset (Wang et al., 2021) and perform relaxations using ASE, recording the throughput and energy MAE for each model. As shown in Figure 5(b), MatRIS achieves a favorable balance between speed and accuracy, maintaining high precision while enabling faster computation.

5 CONCLUSION AND FUTURE WORK

In this work, we review the characteristics of invariant, equivariant and unconstrained MLIPs in the era of rapidly expanding QM-based datasets. Equivariant MLIPs deliver superior accuracy while their reliance on tensor products and high-degree representations leads to prohibitive computational costs. Motivated by the question of whether strict equivariance remains indispensable, we introduce MatRIS, an invariant MLIP that leverages attention to model three-body interactions. Across multiple benchmarks, MatRIS attains SOTA results, opening a new path toward accurate and efficient MLIPs.

In future work, we will scale MatRIS to even larger QM-based datasets to further validate its expressiveness. We aim to develop a reliable distillation strategy to develop student MLIPs. We also plan to expand MatRIS to incorporate long-range electrostatics, thereby enhancing its applicability to more complex downstream tasks.

ACKNOWLEDGMENTS

This work is supported by the following funding: National Science Foundation of China (T2125013, 92270206, 62372435), the Innovation Funding of ICT, CAS. Part of the training is performed on the robotic AI-Scientist platform of Chinese Academy of Sciences. The authors thank the ICT operations team for their strong support.

We thank Duo Zhang for helpful discussions. We also thank Lijun Liu (Osaka University) for evaluating the eqV2 Liao et al. (2024b); Barroso-Luque et al. (2024) and eSEN Fu et al. (2025).

REFERENCES

- Josh Abramson, Jonas Adler, Jack Dunger, Richard Evans, Tim Green, Alexander Pritzel, Olaf Ronneberger, Lindsay Willmore, Andrew J. Ballard, Joshua Bambrick, Sebastian W. Bodenstein, David A. Evans, Chia-Chun Hung, Michael O’Neill, David Reiman, Kathryn Tunyasuvunakool, Zachary Wu, Akvilė Žemgulytė, Eirini Arvaniti, Charles Beattie, Ottavia Bertolli, Alex Bridgland, Alexey Cherepanov, Miles Congreve, Alexander I. Cowen-Rivers, Andrew Cowie, Michael Figurnov, Fabian B. Fuchs, Hannah Gladman, Rishub Jain, Yousuf A. Khan, Caroline M. R. Low, Kuba Perlin, Anna Potapenko, Pascal Savy, Sukhdeep Singh, Adrian Stecula, Ashok Thillaisundaram, Catherine Tong, Sergei Yakneen, Ellen D. Zhong, Michal Zielinski, Augustin Židek, Victor Bapst, Pushmeet Kohli, Max Jaderberg, Demis Hassabis, and John M. Jumper. Accurate structure prediction of biomolecular interactions with AlphaFold 3. *Nature*, 630(8016):493–500, June 2024. ISSN 1476-4687. doi: 10.1038/s41586-024-07487-w. URL <https://doi.org/10.1038/s41586-024-07487-w>.
- Marco Anselmi, Greg Slabaugh, Rachel Crespo-Otero, and Devis Di Tommaso. Molecular graph transformer: stepping beyond alignn into long-range interactions. *Digital Discovery*, 3: 1048–1057, 2024. doi: 10.1039/D4DD00014E. URL <http://dx.doi.org/10.1039/D4DD00014E>.
- Dylan M. Anstine, Roman Zubatyuk, and Olexandr Isayev. Aimnet2: a neural network potential to meet your neutral, charged, organic, and elemental-organic needs. *Chem. Sci.*, 16:10228–10244, 2025. doi: 10.1039/D4SC08572H. URL <http://dx.doi.org/10.1039/D4SC08572H>.
- Sarp Aykent and Tian Xia. Gotennet: Rethinking efficient 3d equivariant graph neural networks. In *The Thirteenth International Conference on Learning Representations*, 2025. URL <https://openreview.net/forum?id=5wxCQDtbMo>.
- Luis Barroso-Luque, Muhammed Shuaibi, Xiang Fu, Brandon M Wood, Misko Dzamba, Meng Gao, Ammar Rizvi, C Lawrence Zitnick, and Zachary W Ulissi. Open materials 2024 (omat24) inorganic materials dataset and models. *arXiv preprint arXiv:2410.12771*, 2024.
- Ilyes Batatia, David Peter Kovacs, Gregor N. C. Simm, Christoph Ortner, and Gabor Csanyi. MACE: Higher order equivariant message passing neural networks for fast and accurate force fields. In Alice H. Oh, Alekh Agarwal, Danielle Belgrave, and Kyunghyun Cho (eds.), *Advances in Neural Information Processing Systems*, 2022. URL <https://openreview.net/forum?id=YpPsnGE-ZU>.
- Simon Batzner, Albert Musaelian, Lixin Sun, Mario Geiger, Jonathan P. Mailoa, Mordechai Kornbluth, Nicola Molinari, Tess E. Smidt, and Boris Kozinsky. E(3)-equivariant graph neural networks for data-efficient and accurate interatomic potentials. *Nature Communications*, 13(1), May 2022. ISSN 2041-1723. doi: 10.1038/s41467-022-29939-5. URL <http://dx.doi.org/10.1038/s41467-022-29939-5>.
- Lennart Bengtsson. Dipole correction for surface supercell calculations. *Phys. Rev. B*, 59:12301–12304, May 1999. doi: 10.1103/PhysRevB.59.12301. URL <https://link.aps.org/doi/10.1103/PhysRevB.59.12301>.
- Filippo Bigi, Marcel F. Langer, and Michele Ceriotti. The dark side of the forces: assessing non-conservative force models for atomistic machine learning. In *Forty-second International Conference on Machine Learning*, 2025.

- Erik Bitzek, Pekka Koskinen, Franz Gähler, Michael Moseler, and Peter Gumbsch. Structural relaxation made simple. *Phys. Rev. Lett.*, 97:170201, Oct 2006. doi: 10.1103/PhysRevLett.97.170201. URL <https://link.aps.org/doi/10.1103/PhysRevLett.97.170201>.
- Rebecca R. Brew, Ian A. Nelson, Meruyert Binayeva, Amlan S. Nayak, Wyatt J. Simmons, Joseph J. Gair, and Corin C. Wagen. Wiggle150: Benchmarking Density Functionals and Neural Network Potentials on Highly Strained Conformers. *Journal of Chemical Theory and Computation*, 21(8):3922–3929, April 2025. ISSN 1549-9618. doi: 10.1021/acs.jctc.5c00015. URL <https://doi.org/10.1021/acs.jctc.5c00015>. Publisher: American Chemical Society.
- Shaked Brody, Uri Alon, and Eran Yahav. How attentive are graph attention networks? In *International Conference on Learning Representations*, 2022. URL <https://openreview.net/forum?id=F72ximsx7C1>.
- Lowik Chanussot, Abhishek Das, Siddharth Goyal, Thibaut Lavril, Muhammed Shuaibi, Morgane Riviere, Kevin Tran, Javier Heras-Domingo, Caleb Ho, Weihua Hu, Aini Palizhati, Anuroop Sriram, Brandon Wood, Junwoong Yoon, Devi Parikh, C. Lawrence Zitnick, and Zachary Ulissi. Open catalyst 2020 (oc20) dataset and community challenges. *ACS Catalysis*, 11(10):6059–6072, May 2021. ISSN 2155-5435. doi: 10.1021/acscatal.0c04525. URL <http://dx.doi.org/10.1021/acscatal.0c04525>.
- Chi Chen and Shyue Ping Ong. A universal graph deep learning interatomic potential for the periodic table. *Nature Computational Science*, 2(11):718–728, November 2022. ISSN 2662-8457. URL <https://doi.org/10.1038/s43588-022-00349-3>.
- Stefan Chmiela, Valentin Vassilev-Galindo, Oliver T. Unke, Adil Kabylda, Huziel E. Sauceda, Alexandre Tkatchenko, and Klaus-Robert Müller. Accurate global machine learning force fields for molecules with hundreds of atoms. *Science Advances*, 9(2):eadf0873, 2023. doi: 10.1126/sciadv.adf0873. URL <https://www.science.org/doi/abs/10.1126/sciadv.adf0873>.
- Kamal Choudhary and Brian DeCost. Atomistic Line Graph Neural Network for improved materials property predictions. *npj Computational Materials*, 7(1):185, November 2021. ISSN 2057-3960. doi: 10.1038/s41524-021-00650-1. URL <https://doi.org/10.1038/s41524-021-00650-1>.
- Kamal Choudhary, Brian DeCost, Lily Major, Keith Butler, Jeyan Thiyagalingam, and Francesca Tavazza. Unified graph neural network force-field for the periodic table: solid state applications. *Digital Discovery*, 2(2):346–355, 2023. ISSN 2635-098X. doi: 10.1039/d2dd00096b. URL <http://dx.doi.org/10.1039/D2DD00096B>.
- Marco De Vivo, Matteo Masetti, Giovanni Bottegoni, and Andrea Cavalli. Role of Molecular Dynamics and Related Methods in Drug Discovery. *Journal of Medicinal Chemistry*, 59(9):4035–4061, 2016.
- Bowen Deng, Peichen Zhong, KyuJung Jun, Janosh Riebesell, Kevin Han, Christopher J. Bartel, and Gerbrand Ceder. Chgnet as a pretrained universal neural network potential for charge-informed atomistic modelling. *Nature Machine Intelligence*, pp. 1–11, 2023. doi: 10.1038/s42256-023-00716-3.
- Bowen Deng, Yunyeong Choi, Peichen Zhong, Janosh Riebesell, Shashwat Anand, Zhuohan Li, KyuJung Jun, Kristin A. Persson, and Gerbrand Ceder. Overcoming systematic softening in universal machine learning interatomic potentials by fine-tuning, 2024. URL <https://arxiv.org/abs/2405.07105>.
- Weitao Du, Yuanqi Du, Limei Wang, Dieqiao Feng, Guifeng Wang, Shuiwang Ji, Carla P Gomes, and Zhi-Ming Ma. A new perspective on building efficient and expressive 3d equivariant graph neural networks. In *Proceedings of the 37th International Conference on Neural Information Processing Systems*. Curran Associates Inc., 2023.
- Alexandre Duval, Simon V. Mathis, Chaitanya K. Joshi, Victor Schmidt, Santiago Miret, Fragkiskos D. Malliaros, Taco Cohen, Pietro Liò, Yoshua Bengio, and Michael Bronstein. A hitchhiker’s guide to geometric gnns for 3d atomic systems, 2024. URL <https://arxiv.org/abs/2312.07511>.

- Zheyong Fan, Yanzhou Wang, Penghua Ying, Keke Song, Junjie Wang, Yong Wang, Zezhu Zeng, Ke Xu, Eric Lindgren, J Magnus Rahm, et al. Gpumd: A package for constructing accurate machine-learned potentials and performing highly efficient atomistic simulations. *The Journal of Chemical Physics*, 157(11), 2022.
- Estefanía Fernández-Villanueva, Pablo G. Lustemberg, Minjie Zhao, Jose Soriano Rodriguez, Patricia Concepción, and M. Verónica Ganduglia-Pirovano. Water and Cu+ Synergy in Selective CO₂ Hydrogenation to Methanol over Cu-MgO-Al₂O₃ Catalysts. *Journal of the American Chemical Society*, 146(3):2024–2032, January 2024. ISSN 0002-7863. doi: 10.1021/jacs.3c10685. URL <https://doi.org/10.1021/jacs.3c10685>. Publisher: American Chemical Society.
- Xiang Fu, Zhenghao Wu, Wujie Wang, Tian Xie, Sinan Ketten, Rafael Gomez-Bombarelli, and Tommi Jaakkola. Forces are not enough: Benchmark and critical evaluation for machine learning force fields with molecular simulations. *Transactions on Machine Learning Research*, 2023. ISSN 2835-8856. URL <https://openreview.net/forum?id=A8pqQipwkt>. Survey Certification.
- Xiang Fu, Brandon M Wood, Luis Barroso-Luque, Daniel S. Levine, Meng Gao, Misko Dzamba, and C. Lawrence Zitnick. Learning smooth and expressive interatomic potentials for physical property prediction. In *Forty-second International Conference on Machine Learning*, 2025. URL <https://openreview.net/forum?id=R0PBjxIbgn>.
- Yuxiang Gao, Fenglin Deng, Ri He, and Zhicheng Zhong. Spontaneous curvature in two-dimensional van der Waals heterostructures. *Nature Communications*, 16(1):717, January 2025. ISSN 2041-1723. doi: 10.1038/s41467-025-56055-x. URL <https://doi.org/10.1038/s41467-025-56055-x>.
- Johannes Gasteiger, Janek Groß, and Stephan Günnemann. Directional message passing for molecular graphs. In *International Conference on Learning Representations*, 2020. URL <https://openreview.net/forum?id=BlEwBxStPH>.
- Johannes Gasteiger, Shankari Giri, Johannes T. Margraf, and Stephan Günnemann. Fast and uncertainty-aware directional message passing for non-equilibrium molecules, 2022a. URL <https://arxiv.org/abs/2011.14115>.
- Johannes Gasteiger, Muhammed Shuaibi, Anuroop Sriram, Stephan Günnemann, Zachary Ward Ulissi, C. Lawrence Zitnick, and Abhishek Das. Gemnet-OC: Developing graph neural networks for large and diverse molecular simulation datasets. *Transactions on Machine Learning Research*, 2022b. ISSN 2835-8856. URL <https://openreview.net/forum?id=u8tvSxm4Bs>.
- Vahe Gharakhanyan, Luis Barroso-Luque, Yi Yang, Muhammed Shuaibi, Kyle Michel, Daniel S. Levine, Misko Dzamba, Xiang Fu, Meng Gao, Xingyu Liu, Haoran Ni, Keian Noori, Brandon M. Wood, Matt Uyttendaele, Arman Boromand, C. Lawrence Zitnick, Noa Marom, Zachary W. Ulissi, and Anuroop Sriram. Open molecular crystals 2025 (omc25) dataset and models, 2025. URL <https://arxiv.org/abs/2508.02651>.
- Jonathan Godwin, Michael Schaarschmidt, Alexander L. Gaunt, Alvaro Sanchez-Gonzalez, Yulia Rubanova, Petar Veličković, James Kirkpatrick, and Peter Battaglia. Simple GNN regularisation for 3d molecular property prediction and beyond. In *International Conference on Learning Representations*, 2022. URL <https://openreview.net/forum?id=1wVvweK3oIb>.
- Frank Harary and Robert Z. Norman. Some properties of line digraphs. *Rendiconti del Circolo Matematico di Palermo*, 9(2):161–168, May 1960. ISSN 1973-4409. doi: 10.1007/BF02854581. URL <https://doi.org/10.1007/BF02854581>.
- Ryan Jacobs, Dane Morgan, Siamak Attarian, Jun Meng, Chen Shen, Zhenghao Wu, Clare Yijia Xie, Julia H. Yang, Nongnuch Artrith, Ben Blaiszik, Gerbrand Ceder, Kamal Choudhary, Gabor Csanyi, Ekin Dogus Cubuk, Bowen Deng, Ralf Drautz, Xiang Fu, Jonathan Godwin, Vasant Honavar, Olexandr Isayev, Anders Johansson, Boris Kozinsky, Stefano Martiniani, Shyue Ping Ong, Igor Poltavsky, KJ Schmidt, So Takamoto, Aidan P. Thompson, Julia Westermayr, and Brandon M. Wood. A practical guide to machine learning interatomic potentials – status and future. *Current Opinion in Solid State and Materials Science*, 35:101214, March 2025. ISSN

1359-0286. doi: 10.1016/j.cossms.2025.101214. URL <http://dx.doi.org/10.1016/j.cossms.2025.101214>.

Anubhav Jain, Shyue Ping Ong, Geoffroy Hautier, Wei Chen, William Davidson Richards, Stephen Dacek, Shreyas Cholia, Dan Gunter, David Skinner, Gerbrand Ceder, and Kristin A. Persson. Commentary: The materials project: A materials genome approach to accelerating materials innovation. *APL Materials*, 1(1):011002, 07 2013a. ISSN 2166-532X. doi: 10.1063/1.4812323. URL <https://doi.org/10.1063/1.4812323>.

Anubhav Jain, Shyue Ping Ong, Geoffroy Hautier, Wei Chen, William Davidson Richards, Stephen Dacek, Shreyas Cholia, Dan Gunter, David Skinner, Gerbrand Ceder, et al. Commentary: The materials project: A materials genome approach to accelerating materials innovation. *APL materials*, 1(1), 2013b.

John Jumper, Richard Evans, Alexander Pritzel, Tim Green, Michael Figurnov, Olaf Ronneberger, Kathryn Tunyasuvunakool, Russ Bates, Augustin Žídek, Anna Potapenko, Alex Bridgland, Clemens Meyer, Simon A. A. Kohl, Andrew J. Ballard, Andrew Cowie, Bernardino Romera-Paredes, Stanislav Nikolov, Rishub Jain, Jonas Adler, Trevor Back, Stig Petersen, David Reiman, Ellen Clancy, Michal Zielinski, Martin Steinegger, Michalina Pacholska, Tamas Berghammer, Sebastian Bodenstern, David Silver, Oriol Vinyals, Andrew W. Senior, Koray Kavukcuoglu, Pushmeet Kohli, and Demis Hassabis. Highly accurate protein structure prediction with AlphaFold. *Nature*, 596(7873):583–589, August 2021. ISSN 1476-4687. doi: 10.1038/s41586-021-03819-2. URL <https://doi.org/10.1038/s41586-021-03819-2>.

Aaron D. Kaplan, Runze Liu, Ji Qi, Tsz Wai Ko, Bowen Deng, Janosh Riebesell, Gerbrand Ceder, Kristin A. Persson, and Shyue Ping Ong. A foundational potential energy surface dataset for materials, 2025. URL <https://arxiv.org/abs/2503.04070>.

Jaesun Kim, Jisu Kim, Jaehoon Kim, Jiho Lee, Yutack Park, Youngho Kang, and Seungwu Han. Data-Efficient Multifidelity Training for High-Fidelity Machine Learning Interatomic Potentials. *Journal of the American Chemical Society*, 147(1):1042–1054, January 2025. ISSN 0002-7863. doi: 10.1021/jacs.4c14455. URL <https://doi.org/10.1021/jacs.4c14455>.

Johannes Klicpera, Florian Becker, and Stephan Günnemann. Gemnet: Universal directional graph neural networks for molecules. In A. Beygelzimer, Y. Dauphin, P. Liang, and J. Wortman Vaughan (eds.), *Advances in Neural Information Processing Systems*, 2021. URL https://openreview.net/forum?id=HS_sOaxS9K-.

Teddy Koker and Tess Smidt. Training a foundation model for materials on a budget, 2025. URL <https://arxiv.org/abs/2508.16067>.

Dávid Péter Kovács, J. Harry Moore, Nicholas J. Browning, Ilyes Batatia, Joshua T. Horton, Yixuan Pu, Venkat Kapil, William C. Witt, Ioan-Bogdan Magdău, Daniel J. Cole, and Gábor Csányi. MACE-OFF: Short-Range Transferable Machine Learning Force Fields for Organic Molecules. *Journal of the American Chemical Society*, 147(21):17598–17611, May 2025. ISSN 0002-7863. doi: 10.1021/jacs.4c07099. URL <https://doi.org/10.1021/jacs.4c07099>.

Thomas D. Kühne and Rustam Z. Khaliullin. Electronic signature of the instantaneous asymmetry in the first coordination shell of liquid water. *Nature Communications*, 4(1):1450, February 2013. ISSN 2041-1723. doi: 10.1038/ncomms2459. URL <https://doi.org/10.1038/ncomms2459>.

Daniel S. Levine, Muhammed Shuaibi, Evan Walter Clark Spotte-Smith, Michael G. Taylor, Muhammad R. Hasyim, Kyle Michel, Ilyes Batatia, Gábor Csányi, Misko Dzamba, Peter Eastman, Nathan C. Frey, Xiang Fu, Vahe Gharakhanyan, Aditi S. Krishnapriyan, Joshua A. Rackers, Sanjeev Raja, Ammar Rizvi, Andrew S. Rosen, Zachary Ulissi, Santiago Vargas, C. Lawrence Zitnick, Samuel M. Blau, and Brandon M. Wood. The open molecules 2025 (omol25) dataset, evaluations, and models, 2025. URL <https://arxiv.org/abs/2505.08762>.

Yi-Lun Liao and Tess Smidt. Equiformer: Equivariant graph attention transformer for 3d atomistic graphs. In *The Eleventh International Conference on Learning Representations*, 2023. URL <https://openreview.net/forum?id=KwmPfARgOTD>.

- Yi-Lun Liao, Tess Smidt, Muhammed Shuaibi, and Abhishek Das. Generalizing denoising to non-equilibrium structures improves equivariant force fields. *Transactions on Machine Learning Research*, 2024a. ISSN 2835-8856. URL <https://openreview.net/forum?id=whGzYUbIWA>.
- Yi-Lun Liao, Brandon M Wood, Abhishek Das, and Tess Smidt. Equiformerv2: Improved equivariant transformer for scaling to higher-degree representations. In *The Twelfth International Conference on Learning Representations*, 2024b. URL <https://openreview.net/forum?id=mCOBKZmrzD>.
- Yi Liu, Limei Wang, Meng Liu, Yuchao Lin, Xuan Zhang, Bora Oztekin, and Shuiwang Ji. Spherical message passing for 3d molecular graphs. In *International Conference on Learning Representations*, 2022. URL <https://openreview.net/forum?id=givsRXsOt9r>.
- Antoine Loew, Dewen Sun, Hai-Chen Wang, Silvana Botti, and Miguel A. L. Marques. Universal machine learning interatomic potentials are ready for phonons. *npj Computational Materials*, 11(1):178, June 2025. ISSN 2057-3960. doi: 10.1038/s41524-025-01650-1. URL <https://doi.org/10.1038/s41524-025-01650-1>.
- Nataliya Lopanitsyna, Guillaume Fraux, Maximilian A. Springer, Sandip De, and Michele Ceriotti. Modeling high-entropy transition metal alloys with alchemical compression. *Phys. Rev. Mater.*, 7:045802, Apr 2023. doi: 10.1103/PhysRevMaterials.7.045802. URL <https://link.aps.org/doi/10.1103/PhysRevMaterials.7.045802>.
- Arslan Mazitov, Filippo Bigi, Matthias Kellner, Paolo Pegolo, Davide Tisi, Guillaume Fraux, Sergey Pozdnyakov, Philip Loche, and Michele Ceriotti. Pet-mad, a lightweight universal interatomic potential for advanced materials modeling, 2025. URL <https://arxiv.org/abs/2503.14118>.
- Amil Merchant, Simon Batzner, Samuel S. Schoenholz, Muratahan Aykol, Gowoon Cheon, and Ekin Dogus Cubuk. Scaling deep learning for materials discovery. *Nature*, 624(7990):80–85, 2023.
- Albert Musaelian, Simon Batzner, Anders Johansson, Lixin Sun, Cameron J. Owen, Mordechai Kornbluth, and Boris Kozinsky. Learning local equivariant representations for large-scale atomistic dynamics. *Nature Communications*, 14(1):579, February 2023. ISSN 2041-1723. doi: 10.1038/s41467-023-36329-y. URL <https://doi.org/10.1038/s41467-023-36329-y>.
- Mark Neumann, James Gin, Benjamin Rhodes, Steven Bennett, Zhiyi Li, Hitarth Choubisa, Arthur Hussey, and Jonathan Godwin. Orb: A fast, scalable neural network potential, 2024. URL <https://arxiv.org/abs/2410.22570>.
- Ivan S Novikov, Konstantin Gubaev, Evgeny V Podryabinkin, and Alexander V Shapeev. The mlp package: moment tensor potentials with mpi and active learning. *Machine Learning: Science and Technology*, 2(2):025002, dec 2020. doi: 10.1088/2632-2153/abc9fe. URL <https://dx.doi.org/10.1088/2632-2153/abc9fe>.
- Yutack Park, Jaesun Kim, Seungwoo Hwang, and Seungwu Han. Scalable parallel algorithm for graph neural network interatomic potentials in molecular dynamics simulations. *Journal of Chemical Theory and Computation*, 20(11):4857–4868, May 2024. ISSN 1549-9626. doi: 10.1021/acs.jctc.4c00190. URL <http://dx.doi.org/10.1021/acs.jctc.4c00190>.
- Anyang Peng, Chun Cai, Mingyu Guo, Duo Zhang, Chengqian Zhang, Wanrun Jiang, Yinan Wang, Antoine Loew, Chengkun Wu, Weinan E, Linfeng Zhang, and Han Wang. LAMBench: a benchmark for large atomistic models. *npj Computational Materials*, 12(1):62, January 2026. ISSN 2057-3960. doi: 10.1038/s41524-025-01929-3. URL <https://doi.org/10.1038/s41524-025-01929-3>.
- Sergey N. Pozdnyakov and Michele Ceriotti. Smooth, exact rotational symmetrization for deep learning on point clouds. In *Proceedings of the 37th International Conference on Neural Information Processing Systems*, NIPS '23, Red Hook, NY, USA, 2023. Curran Associates Inc.

- Balázs Póta, Paramvir Ahlawat, Gábor Csányi, and Michele Simoncelli. Thermal conductivity predictions with foundation atomistic models, 2025. URL <https://arxiv.org/abs/2408.00755>.
- Eric Qu and Aditi S. Krishnapriyan. The importance of being scalable: Improving the speed and accuracy of neural network interatomic potentials across chemical domains. In *The Thirty-eighth Annual Conference on Neural Information Processing Systems*, 2024. URL <https://openreview.net/forum?id=Y4mBaZu4vy>.
- Benjamin Rhodes, Sander Vandenhaute, Vaidotas Šimkus, James Gin, Jonathan Godwin, Tim Duignan, and Mark Neumann. Orb-v3: atomistic simulation at scale, 2025. URL <https://arxiv.org/abs/2504.06231>.
- Janosh Riebesell, Rhys E. A. Goodall, Philipp Benner, Yuan Chiang, Bowen Deng, Gerbrand Ceder, Mark Asta, Alpha A. Lee, Anubhav Jain, and Kristin A. Persson. A framework to evaluate machine learning crystal stability predictions. *Nature Machine Intelligence*, 7(6):836–847, 2025.
- Jonathan Schmidt, Tiago F.T. Cerqueira, Aldo H. Romero, Antoine Loew, Fabian Jäger, Hai-Chen Wang, Silvana Botti, and Miguel A.L. Marques. Improving machine-learning models in materials science through large datasets. *Materials Today Physics*, 48:101560, 2024. ISSN 2542-5293. doi: <https://doi.org/10.1016/j.mtphys.2024.101560>.
- K. T. Schütt, P.-J. Kindermans, H. E. Saucedo, S. Chmiela, A. Tkatchenko, and K.-R. Müller. Schnet: a continuous-filter convolutional neural network for modeling quantum interactions. In *Proceedings of the 31st International Conference on Neural Information Processing Systems, NIPS’17*, pp. 992–1002, Red Hook, NY, USA, 2017. Curran Associates Inc. ISBN 9781510860964.
- Kristof T. Schütt, Oliver T. Unke, and Michael Gastegger. Equivariant message passing for the prediction of tensorial properties and molecular spectra, 2021. URL <https://arxiv.org/abs/2102.03150>.
- Shihao Shao, Haoran Geng, Zun Wang, and Qinghua Cui. FreeCG: Free the design space of clebsch-gordan transform for machine learning force fields. In *The Thirteenth International Conference on Learning Representations*, 2025. URL <https://openreview.net/forum?id=sfi2j10t6j>.
- Justin S. Smith, Ben Nebgen, Nicholas Lubbers, Olexandr Isayev, and Adrian E. Roitberg. Less is more: Sampling chemical space with active learning. *The Journal of Chemical Physics*, 148(24):241733, 05 2018. ISSN 0021-9606. doi: 10.1063/1.5023802. URL <https://doi.org/10.1063/1.5023802>.
- Tyler G. Sours and Ambarish R. Kulkarni. Predicting Structural Properties of Pure Silica Zeolites Using Deep Neural Network Potentials. *The Journal of Physical Chemistry C*, 127(3):1455–1463, January 2023. ISSN 1932-7447. doi: 10.1021/acs.jpcc.2c08429. URL <https://doi.org/10.1021/acs.jpcc.2c08429>. Publisher: American Chemical Society.
- Anuroop Sriram, Logan M. Brabson, Xiaohan Yu, Sihoon Choi, Kareem Abdelmaqsoud, Elias Moubarak, Pim de Haan, Sindy Löwe, Johann Brehmer, John R. Kitchin, Max Welling, C. Lawrence Zitnick, Zachary Ulissi, Andrew J. Medford, and David S. Sholl. The open dac 2025 dataset for sorbent discovery in direct air capture, 2025. URL <https://arxiv.org/abs/2508.03162>.
- Philipp Thölke and Gianni De Fabritiis. Equivariant transformers for neural network based molecular potentials. In *International Conference on Learning Representations*, 2022. URL <https://openreview.net/forum?id=zNHZqZ9wrRB>.
- Atsushi Togo. Phonon database. URL <https://doi.org/10.48505/nims.4197>.
- A. Torres, F. J. Luque, J. Tortajada, and M. E. Arroyo-de Dompablo. Analysis of Minerals as Electrode Materials for Ca-based Rechargeable Batteries. *Scientific Reports*, 9(1):9644, July 2019. ISSN 2045-2322. doi: 10.1038/s41598-019-46002-4. URL <https://doi.org/10.1038/s41598-019-46002-4>.

- Richard Tran, Janice Lan, Muhammed Shuaibi, Brandon M. Wood, Siddharth Goyal, Abhishek Das, Javier Heras-Domingo, Adeesh Kolluru, Ammar Rizvi, Nima Shoghi, Anuroop Sriram, Félix Therrien, Jehad Abed, Oleksandr Voznyy, Edward H. Sargent, Zachary Ulissi, and C. Lawrence Zitnick. The open catalyst 2022 (oc22) dataset and challenges for oxide electrocatalysts. *ACS Catalysis*, 13(5):3066–3084, February 2023. ISSN 2155-5435. doi: 10.1021/acscatal.2c05426. URL <http://dx.doi.org/10.1021/acscatal.2c05426>.
- Oliver T. Unke and Markus Meuwly. Physnet: A neural network for predicting energies, forces, dipole moments, and partial charges. *Journal of Chemical Theory and Computation*, 15(6):3678–3693, May 2019. ISSN 1549-9626. doi: 10.1021/acs.jctc.9b00181. URL <http://dx.doi.org/10.1021/acs.jctc.9b00181>.
- Jonathan Vandermause, Yu Xie, Jin Soo Lim, Cameron J. Owen, and Boris Kozinsky. Active learning of reactive Bayesian force fields applied to heterogeneous catalysis dynamics of H/Pt. *Nature Communications*, 13(1):5183, September 2022. ISSN 2041-1723. doi: 10.1038/s41467-022-32294-0. URL <https://doi.org/10.1038/s41467-022-32294-0>.
- Ashish Vaswani, Noam Shazeer, Niki Parmar, Jakob Uszkoreit, Llion Jones, Aidan N. Gomez, Lukasz Kaiser, and Illia Polosukhin. Attention is all you need, 2023. URL <https://arxiv.org/abs/1706.03762>.
- Brook Wander, Muhammed Shuaibi, John R. Kitchin, Zachary W. Ulissi, and C. Lawrence Zitnick. CatTSunami: Accelerating Transition State Energy Calculations with Pretrained Graph Neural Networks. *ACS Catalysis*, 15(7):5283–5294, April 2025. doi: 10.1021/acscatal.4c04272. URL <https://doi.org/10.1021/acscatal.4c04272>.
- Hai-Chen Wang, Silvana Botti, and Miguel A. L. Marques. Predicting stable crystalline compounds using chemical similarity. *npj Computational Materials*, 7(1):12, January 2021. ISSN 2057-3960. doi: 10.1038/s41524-020-00481-6. URL <https://doi.org/10.1038/s41524-020-00481-6>.
- Limei Wang, Yi Liu, Yuchao Lin, Haoran Liu, and Shuiwang Ji. Comenet: towards complete and efficient message passing for 3d molecular graphs. In *Proceedings of the 36th International Conference on Neural Information Processing Systems, NIPS '22*, Red Hook, NY, USA, 2022. Curran Associates Inc. ISBN 9781713871088.
- Tong Wang, Xinheng He, Mingyu Li, Bin Shao, and Tie-Yan Liu. AIMD-Chig: Exploring the conformational space of a 166-atom protein Chignolin with ab initio molecular dynamics. *Scientific Data*, 10(1):549, August 2023. ISSN 2052-4463. doi: 10.1038/s41597-023-02465-9. URL <https://doi.org/10.1038/s41597-023-02465-9>.
- Yusong Wang, Tong Wang, Shaoning Li, Xinheng He, Mingyu Li, Zun Wang, Nanning Zheng, Bin Shao, and Tie-Yan Liu. Enhancing geometric representations for molecules with equivariant vector-scalar interactive message passing. *Nature Communications*, 15(1):313, January 2024. ISSN 2041-1723. doi: 10.1038/s41467-023-43720-2. URL <https://doi.org/10.1038/s41467-023-43720-2>.
- Hassler Whitney. *Congruent Graphs and the Connectivity of Graphs*, pp. 61–79. Birkhäuser Boston, Boston, MA, 1992. doi: 10.1007/978-1-4612-2972-8_4. URL https://doi.org/10.1007/978-1-4612-2972-8_4.
- Brandon M. Wood, Misko Dzamba, Xiang Fu, Meng Gao, Muhammed Shuaibi, Luis Barroso-Luque, Kareem Abdelmaqsoud, Vahe Gharakhanyan, John R. Kitchin, Daniel S. Levine, Kyle Michel, Anuroop Sriram, Taco Cohen, Abhishek Das, Ammar Rizvi, Sushree Jagriti Sahoo, Zachary W. Ulissi, and C. Lawrence Zitnick. Uma: A family of universal models for atoms, 2025.
- Tian Xie and Jeffrey C. Grossman. Crystal graph convolutional neural networks for an accurate and interpretable prediction of material properties. *Physical Review Letters*, 120(14), April 2018. ISSN 1079-7114. doi: 10.1103/physrevlett.120.145301. URL <http://dx.doi.org/10.1103/PhysRevLett.120.145301>.

- Keyulu Xu, Weihua Hu, Jure Leskovec, and Stefanie Jegelka. How powerful are graph neural networks?, 2019. URL <https://arxiv.org/abs/1810.00826>.
- Han Yang, Chenxi Hu, Yichi Zhou, Xixian Liu, Yu Shi, Jielan Li, Guanzhi Li, Zekun Chen, Shuizhou Chen, Claudio Zeni, Matthew Horton, Robert Pinsler, Andrew Fowler, Daniel Zügner, Tian Xie, Jake Smith, Lixin Sun, Qian Wang, Lingyu Kong, Chang Liu, Hongxia Hao, and Ziheng Lu. Mattersim: A deep learning atomistic model across elements, temperatures and pressures, 2024.
- M. Yang, D. Zhang, X. Wang, B. Li, L. Zhang, W. E, T. Zhu, and H. Wang. Ab initio accuracy neural network potential for drug-like molecules. 2025. doi: 10.34133/research.0837.
- Bangchen Yin, Jiaao Wang, Weitao Du, Pengbo Wang, Penghua Ying, Haojun Jia, Zisheng Zhang, Yuanqi Du, Carla Gomes, Chenru Duan, Graeme Henkelman, and Hai Xiao. AlphaNet: scaling up local-frame-based neural network interatomic potentials. *npj Computational Materials*, 11(1): 332, November 2025. ISSN 2057-3960. doi: 10.1038/s41524-025-01817-w. URL <https://doi.org/10.1038/s41524-025-01817-w>.
- Sheheryar Zaidi, Michael Schaarschmidt, James Martens, Hyunjik Kim, Yee Whye Teh, Alvaro Sanchez-Gonzalez, Peter Battaglia, Razvan Pascanu, and Jonathan Godwin. Pre-training via denoising for molecular property prediction. In *The Eleventh International Conference on Learning Representations*, 2023. URL <https://openreview.net/forum?id=tYIMtogyee>.
- Duo Zhang, Xinzijian Liu, Xiangyu Zhang, Chengqian Zhang, Chun Cai, Hangrui Bi, Yiming Du, Xuejian Qin, Anyang Peng, Jiameng Huang, Bowen Li, Yifan Shan, Jinzhe Zeng, Yuzhi Zhang, Siyuan Liu, Yifan Li, Junhan Chang, Xinyan Wang, Shuo Zhou, Jianchuan Liu, Xiaoshan Luo, Zhenyu Wang, Wanrun Jiang, Jing Wu, Yudi Yang, Jiyuan Yang, Manyi Yang, Fu-Qiang Gong, Linshuang Zhang, Mengchao Shi, Fu-Zhi Dai, Darrin M. York, Shi Liu, Tong Zhu, Zhicheng Zhong, Jian Lv, Jun Cheng, Weile Jia, Mohan Chen, Guolin Ke, Weinan E, Linfeng Zhang, and Han Wang. DPA-2: a large atomic model as a multi-task learner. *npj Computational Materials*, 10(1):293, 2024.
- Duo Zhang, Anyang Peng, Chun Cai, Wentao Li, Yuanchang Zhou, Jinzhe Zeng, Mingyu Guo, Chengqian Zhang, Bowen Li, Hong Jiang, Tong Zhu, Weile Jia, Linfeng Zhang, and Han Wang. A graph neural network for the era of large atomistic models, 2025.
- Yaolong Zhang, Xueyao Zhou, and Bin Jiang. Bridging the Gap between Direct Dynamics and Globally Accurate Reactive Potential Energy Surfaces Using Neural Networks. *The Journal of Physical Chemistry Letters*, 10(6):1185–1191, March 2019. doi: 10.1021/acs.jpcllett.9b00085. URL <https://doi.org/10.1021/acs.jpcllett.9b00085>. Publisher: American Chemical Society.

APPENDIX

A Additional related works

A.1 Explicit three-body modeling in MLIPs

A.2 Attention-based MLIPs

B Details of MatRIS

C Training strategies

C.1 Load-balance strategy

C.2 Loss-balance strategy

C.3 Details of denoising pretraining

D Additional evaluation

D.1 Matbench-Discovery benchmark (non-compliant)

D.2 LAMBench benchmark

D.3 Zeolite benchmark

D.4 DPA2 test sets

D.5 MD stability evaluation

E Training details and hyper-parameters

A ADDITIONAL RELATED WORKS

A.1 EXPLICIT THREE-BODY MODELING IN MLIPs

Three-body information is important for predicting various material properties (Choudhary & DeCost, 2021; Choudhary et al., 2023; Zhang et al., 2025). Several MLIPs explicitly model three-body interactions, including the ALIGNN series (Choudhary & DeCost, 2021; Choudhary et al., 2023), DimeNet series (Gasteiger et al., 2020; 2022a), GemNet series (Gasteiger et al., 2022b; Klicpera et al., 2021), M3GNet series (Chen & Ong, 2022; Yang et al., 2024), and DPA3 (Zhang et al., 2025), where three-body features are updated within the interaction block and then used to refine edge and node features. MatRIS also explicitly models three-body interactions, but differs in its update and aggregation strategy:

1. In MatRIS, three-body features are updated using an attention mechanism with $O(N)$ complexity, which improves model accuracy while maintaining computational efficiency (see Table 4(a), Index 1 and 3).
2. During message aggregation, a learnable envelope function is used to smooth the three-body contributions, instead of using a simple distance-based attenuation. This design yields better performance (see Table 4(a), Index 3 and 4).

Beyond the above distinctions, MatRIS also achieves SOTA or near-SOTA performance across multiple benchmarks. Notably, on Matbench-Discovery (Riebesell et al., 2025), MatRIS-M attains accuracy comparable to eSEN-30M-MP but with significantly fewer parameters and substantially lower

training cost. This demonstrates the effectiveness of combining three-body interaction modeling with attention mechanisms for materials modeling.

A.2 ATTENTION-BASED MLIPS

Full Attention MLIPs. In potential energy surface modeling, full-attention methods have been widely used, with representative models including DPA2 (Zhang et al., 2024), PET (Pozdnyakov & Ceriotti, 2023), and EScAIP (Qu & Krishnapriyan, 2024). In these models, all features are concatenated into a message tensor of shape $[\text{natoms}, \text{neighbors}, D]$, where D is the hidden dimension, and updated using a full attention mechanism (Vaswani et al., 2023). This mechanism can fully leverage information from neighboring atoms and enable feature interactions. However, due to the $O(N^2)$ computational cost of full attention, the computation quickly becomes expensive as the system size grows. To maintain efficiency, these MLIPs typically consider only two-body interactions.

In contrast, MatRIS employs an attention mechanism with $O(N)$ complexity to capture both two-body and three-body interactions. This allows MatRIS to incorporate more geometric information and enhance the model’s expressive power while maintaining computational efficiency.

Linear-Complexity Attention MLIPs. Although there exist many MLIPs with attention mechanisms of $O(N)$ complexity, such as Equiformer (Liao & Smidt, 2023), ViSNet (Wang et al., 2024), FreeCG (Shao et al., 2025), and MGT (Anselmi et al., 2024), we note that these architectures still differ from MatRIS in several technical aspects.

First, Equiformer is a high-degree steerable equivariant MLIP that employs multi-layer perceptron attention (Liao & Smidt, 2023; Brody et al., 2022) for feature encoding, with $O(N)$ complexity, and can support vectors of any degree L . However, unlike MatRIS, its attention mechanism is not directly used to encode three-body interactions and only considers the source-to-target direction.

ViSNet and FreeCG belong to equivariant MLIPs. Their attention mechanisms can capture up to four-body interactions and also have $O(N)$ complexity. Nevertheless, their technical approaches differ fundamentally from that of MatRIS: ViSNet and FreeCG implicitly extract and refine three- or four-body features, without directly employing attention to encode and update such features. In contrast, MatRIS explicitly extracts three-body features and utilizes attention mechanisms to encode and update them.

It is also worth noting that MGT employs attention and explicitly extracts three-body features. Nevertheless, its attention mechanism operates on node and edge feature updates, and relies on the ALIGNN module (Choudhary & DeCost, 2021) to further refine three-body features. Similar to ViSNet and FreeCG, MGT leverages attention to refine three-body features rather than directly encode them.

In contrast to all the above attention-based models, MatRIS introduces a separable attention mechanism that explicitly models three-body interactions. Its key innovations include:

1. **Dimension-wise:** the attention weights vary across feature dimensions, distinguishing the relative importance of different dimensions.
2. **Separable:** it considers both source-to-target and target-to-source directions, generating separate attention weights for each direction.
3. **Explicit and efficient modeling:** due to its $O(N)$ complexity, MatRIS can efficiently and explicitly encode and update three-body features, thereby significantly enhancing the model’s expressive power.

B DETAILS OF MATRIS

For completeness, in this section we present the details of MatRIS. Given a material graph $G = (Z, X, L)$, the atomic numbers are denoted as $Z \in \mathbb{R}^{\text{natoms} \times 1}$, the atomic positions as $X \in \mathbb{R}^{\text{natoms} \times 3}$, and the lattice as $L \in \mathbb{R}^{3 \times 3}$. In **Graph Generation** (see Figure 6), we first perform periodic repetition, and then construct the Atom Graph G^a and the Line Graph G^l based on radial cutoffs r_{cut}^a and r_{cut}^l , respectively. We typically set $r_{cut}^l < r_{cut}^a$ for computational efficiency.

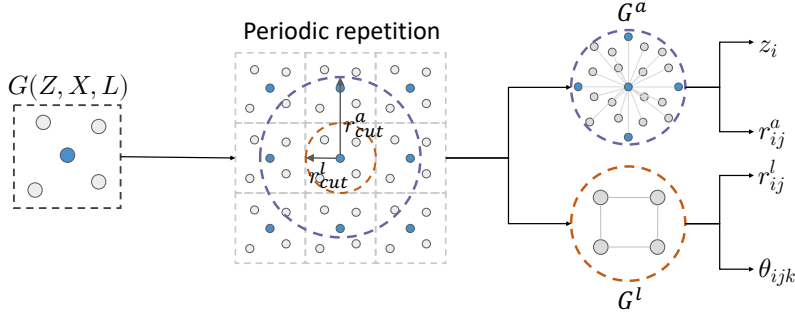


Figure 6: The detail of Graph Generation.

In **Feature Embedding**, the atomic types z_i are expanded using a learnable embedding matrix $A \in \mathbb{R}^{\max_{\text{element}} \times D}$ (see Equation 5). Following Gasteiger et al. (2020), the pairwise distances r_{ij}^a of G^a are expanded with Bessel basis functions, and smoothed with an envelope function ($\mu(r_{ij})$) to ensure that pairwise interactions decay smoothly to zero at the cutoff radius, as shown in Equation 6. For the initialization of three-body interactions θ_{ijk} , we follow Deng et al. (2023) and employ the computationally simpler Fourier basis instead of spherical harmonics (we also tested spherical harmonics but observed no change in accuracy), as shown in Equation 7. Finally, all initialized features undergo nonlinear transformations and are projected into a higher-dimensional space.

$$v_i^0 = W(z_i A) + b \quad (5)$$

$$e_{ij}^0 = \mu(r_{ij}^a) \cdot \sqrt{\frac{2}{r_a}} \frac{\sin\left(\frac{n\pi}{r_a} r_{ij}^a\right)}{r_{ij}^a} \quad (6)$$

$$a_{ijk,m}^0 = \begin{cases} \frac{1}{\sqrt{\pi}} \cos[m\theta_{ijk}], & m \in [0, M_{max}/2], \\ \frac{1}{\sqrt{\pi}} \sin[(m - M_{max}/2)\theta_{ijk}], & m \in [M_{max}/2 + 1, M_{max}]. \end{cases} \quad (7)$$

In the **Graph Attention** module, we consider the n -th layer, which contains the Atom Graph G^a with features v_i^n and e_{ij}^n , and the Line Graph G^l with features e_{ij}^n and θ_{ijk}^n . The two graphs share the edge features e_{ij}^n . To fuse information between the graphs, we first update G^l and then incorporate its output into G^a to aid atomic feature updates (see Equation 8). Specifically, e_{ij}^n and θ_{ijk}^n are input to the ‘Line Graph Attention’ module, producing $e'_{ij,l}{}^{(n)}$ and $\theta'_{ijk}{}^{(n)}$. The updated edge feature $e'_{ij}{}^{(n)}$ encodes three-body interactions and is combined with v_i^n as input to the ‘Atom Graph Attention’ module, yielding $v_i'{}^{(n)}$ and $e_{ij}'{}^{(n)}$.

$$\begin{aligned} e'_{ij,l}{}^{(n)}, \theta'_{ijk}{}^{(n)} &\leftarrow \text{Line Graph Attention}(e_{ij}^n, \theta_{ijk}^n) \\ v_i'{}^{(n)}, e_{ij}'{}^{(n)} &\leftarrow \text{Atom Graph Attention}(v_i^n, e'_{ij,l}{}^{(n)}) \end{aligned} \quad (8)$$

Notably, in G^a , atoms are treated as nodes and pairwise distances as edges, whereas in G^l , pairwise distances are treated as nodes and three-body interactions as edges. Therefore, the computation of the Line Graph Attention and Atom Graph Attention follows the same computation, differing only in their inputs. Here, we take the update of G^a as an example and present the detailed operations of the Graph Attention module.

Given the input of the current attention layer, v_i and e_{ij} (for simplicity, we denote v_i^n and $e'_{ij,l}{}^{(n)}$ as v_i and e_{ij}), we first generate the fusion feature:

$$e'_{ij} = \text{gMLP}(v_i || v_j || e_{ij}) \quad (9)$$

Meanwhile, e_{ij} undergoes two nonlinear transformations. It is then passed through Dim-wise Softmax to get the attention weights for the source and target nodes, sa_{ij} and ta_{ij} . These weights are

then element-wise multiplied with e'_{ij} and fused to produce the output of the attention layer, v'_i , as shown in the equation:

$$\begin{aligned}
 tv_i &= \sum_{k \in \mathcal{N}(i)} (ta_{kj} \odot e'_{kj}), & sv_i &= \sum_{k \in \mathcal{N}(j)} (sa_{kj} \odot e'_{kj}) \\
 v'_i &= \text{gMLP}(tv_i || sv_i)
 \end{aligned}
 \tag{10}$$

After the Attention layer, we employ a **Refinement** layer to further enhance the geometric encodings. In this module, we also apply a learnable envelope function to smooth the potential energy surface. As before, we first update G^l and then G^a . Taking the update of G^a as an example, the inputs are v'_i and e'_{ij} , and we fuse the features from the attention layer:

$$m_{ij}^{(n)} = \text{gMLP}(v'_i || v'_j || e'_{ij}) \tag{11}$$

The fusion feature $m_{ij}^{(n)}$ is transformed nonlinearly to yield the edge update Δe_{ij} . For the node update Δv_i , we first apply the learnable envelope function (Equation 12), then aggregate, and finally apply a nonlinear transformation.

$$\mu_{ij}^{(n)} = \text{Linear}(e_{ij}^0) \tag{12}$$

$$\Delta v_i = \text{MLP}\left(\sum_{k \in \mathcal{N}(i)} (\mu_{ij}^{(n)} \odot m_{ij}^{(n)})\right) \tag{13}$$

$$\Delta e_{ij} = \text{MLP}(m_{ij}^{(n)})$$

In the Readout block, the final atom features $v_i^{(N)}$ are used to directly predict the total energy (E) and magnetic moments (M):

$$E = \sum_i \text{MLP}(v_i^N) + \text{ref}(z_i) \tag{14}$$

$$M = \text{MLP}(v_i^N)$$

Here, $\text{ref}(z_i)$ is obtained by performing a least-squares fit to the dataset energies. The atomic forces F_i and stress (σ) are obtained via automatic differentiation of the energy with respect to the atomic Cartesian coordinates X_i and the lattice strain tensor (ϵ).

$$F_i = -\frac{\partial E}{\partial X_i}, \quad \sigma = \frac{1}{V} \frac{\partial E}{\partial \epsilon} \tag{15}$$

C TRAINING STRATEGIES

C.1 LOAD-BALANCE STRATEGY

In most atomic datasets, the sizes of structures typically follow a long-tailed distribution (Deng et al., 2023; Barroso-Luque et al., 2024). Figure 7(a) visualizes the distributions of atom and edge counts in the MPTrj dataset (cutoff radius 6.0). In distributed training, allocating samples with a fixed batch size may cause two issues: (1) a GPU may receive only large samples, leading to out-of-memory (OOM) and limiting the maximum batch size; (2) assuming memory allows, some GPUs may have higher computational loads while others have lower loads, causing idle time and extra synchronization overhead. To address this, we adopt a **load balancing strategy**:

1. Shuffle the entire dataset to ensure randomness, then split it into multiple chunks.
2. Within each chunk, sort samples in descending order of size.
3. Using a greedy algorithm, assign samples sequentially to GPUs, prioritizing the GPU with the largest remaining capacity. If all GPUs are “full” or the chunk has no remaining samples, a batch is generated.

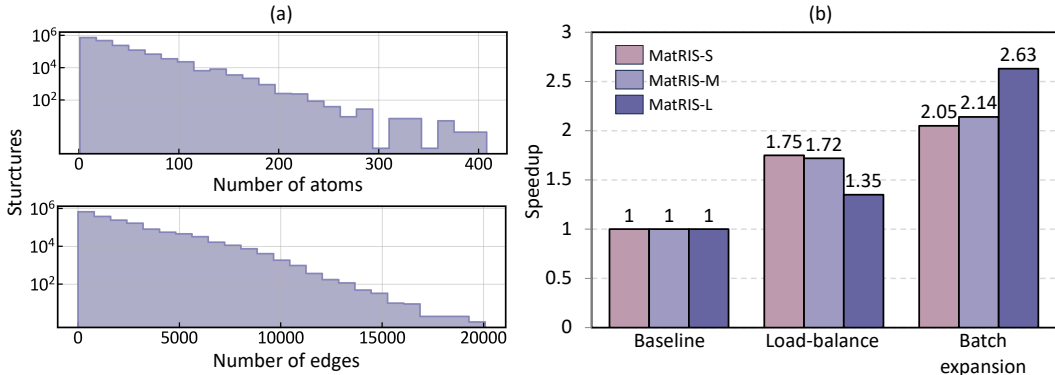


Figure 7: (a)Number of atoms and edges in MPTrj dataset. (b)Training speedup achieved by load balancing.

As shown in Figure 7(b), with load balancing, the cumulative speedup reaches **1.35–1.75** \times , indicating that synchronization overhead due to load imbalance is significant during each training step. Building on this, the global batch size can be increased (denoted as “Batch expansion”), resulting in a cumulative speedup of **2.05–2.63** \times .

C.2 LOSS-BALANCE STRATEGY

Besides load imbalance during training, the loss computation can also be imbalanced. This is especially clear for the force and magmom loss(e.g., node-level tasks). For example, the MSE loss (forces only) is defined as:

$$L_f = \frac{1}{3N_B} \sum_{i=1}^{N_B} \left| f_i^{\text{pred}} - f_i^{\text{DFT}} \right|^2 \quad (16)$$

where N_B denotes the total number of atoms in this global batch.

This reduction method causes the losses of large samples to dominate during training, effectively making the model prioritize large samples and resulting in a loss imbalance. To address this, we adopt a graph-level loss reduction strategy (referred to as **Graph-level loss**). Specifically, when computing node-level losses such as force or magmom, we first reduce the loss within each graph, and then perform a second reduction across the global batch, thereby mitigating the loss imbalance. Ablation studies in Table 4(b) demonstrate the effectiveness of this method. The corresponding formula is as follows:

$$L_f = \frac{1}{B} \sum_{b=1}^B \left(\frac{1}{N_b} \sum_{i=1}^{N_b} \left\| f_i^{\text{pred}} - f_i^{\text{DFT}} \right\|^2 \right) \quad (17)$$

where B is the number of graphs in this global batch, N_b is the number of atoms in the b -th graph.

C.3 DETAILS OF DENOISING PRETRAINING

In this section, we present the denoising strategy used in our work. Several studies, such as Noisy Node (Godwin et al., 2022) and DeNS (Liao et al., 2024a), have demonstrated that denoising can mitigate the over-smoothing of GNNs and improve generalization. However, these methods have restricted applicability. For example, Noisy Node must be applied to equilibrium structures, while DeNS extends it to non-equilibrium states but is limited to equivariant neural networks. In practice, most mainstream atomic datasets are not fully in equilibrium (Deng et al., 2023; Schmidt et al., 2024; Barroso-Luque et al., 2024), and MLIPs are not necessarily equivariant GNNs. The training of MatRIS faces this scenario. For non-equivariant GNNs on non-equilibrium structures, a key challenge in applying denoising is how to encode forces. Inspired by Liao et al. (2024a), we project forces onto edges to scalarize the vectors. The detailed denoising strategy is described step by step as follows:

1. Given a corruption probability, we randomly select atoms to corrupt.

2. For each corrupted atom, we project its force onto the relative position edges by computing inner products, resulting in a scalarized force feature $F(\text{projected})$.
3. We sample a random timestep t and obtain the noise standard deviation σ_t from a linear schedule. We then add noise as $\sigma_t \epsilon$, where ϵ is standard Gaussian noise.
4. The noisy structure, the projected force $F(\text{projected})$, and the timestep t are used as inputs to the MatRIS model, which directly predicts the added Gaussian noise.

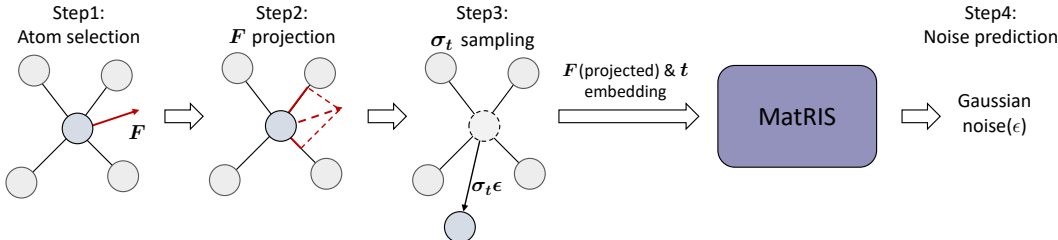


Figure 8: The workflow of denoising pretraining on MatRIS.

The overall workflow is illustrated in Figure 8. After the denoising pretraining stage, the model is further fine-tuned using the pretrained weights.

D ADDITIONAL EVALUATION

D.1 MATBENCH-DISCOVERY BENCHMARK (NON-COMPLIANT)

We report the performance of non-compliant MatRIS-10M-OAM models, all of which were accessed before September 24, 2025. In this benchmark, the training data for each model is not restricted. We follow the setup used by most models, with pretraining on the OMat24 (Barroso-Luque et al., 2024) dataset and joint fine-tuning with sAlex (Schmidt et al., 2024; Barroso-Luque et al., 2024) and MPTrj (Deng et al., 2023). Results on the full, unique, and 10k most stable splits are shown in Table 5, Table 6, and Table 7, respectively. Although MatRIS-10M-OAM has fewer parameters than most models, it still delivers competitive performance across all splits.

Table 5: MatRIS performance on the non-compliant Matbench-Discovery benchmark with results on **full test set**.

Model	Param.	F1 \uparrow	DAF \uparrow	Precision \uparrow	Recall \uparrow	Accuracy \uparrow	MAE \downarrow	R2 \uparrow	RMSD \downarrow
GRACE-2L-OAM-L	26.4M	0.862	5.093	0.874	0.851	0.953	0.022	0.856	0.064
DPA3-3M-FT	3.27M	0.864	4.912	0.843	0.887	0.952	0.022	<u>0.862</u>	0.069
Nequip-OAM-L	9.6M	0.870	5.060	0.868	0.872	0.955	0.022	0.858	0.065
Allegro-OAM-L	9.7M	0.873	4.876	0.837	0.912	0.954	0.021	0.861	0.065
AlphaNet-v1-OMA	4.65M	0.883	5.000	0.858	<u>0.910</u>	0.959	0.023	0.827	0.079
SevenNet-MF-ompa	25.7M	0.884	5.082	0.872	0.895	0.960	0.021	0.861	0.064
ORB v3	25.5M	0.887	5.159	0.885	0.888	0.961	0.023	0.820	0.075
eqV2 M	86.6M	0.896	5.243	0.900	0.893	<u>0.965</u>	0.020	0.842	0.069
eSEN-30M-OAM	30.2M	<u>0.902</u>	5.281	0.906	0.899	0.967	0.018	0.860	<u>0.061</u>
MatRIS-10M-OAM	10.4M	0.903	<u>5.275</u>	<u>0.905</u>	0.901	0.967	<u>0.019</u>	0.864	0.060

D.2 LAMBENCH BENCHMARK

We evaluated the performance of MatRIS-10M-OAM on LAMBench benchmark (Peng et al., 2026), which mainly tests the generalizability of MLIPs. The benchmark covers test domains including molecules, inorganic materials, and catalysis, and includes tasks such as force field prediction and property calculation.

Table 6: MatRIS performance on the non-compliant Matbench-Discovery benchmark with results on **unique structure prototypes**.

Model	Param.	F1↑	DAF↑	Precision↑	Recall↑	Accuracy↑	MAE↓	R2↑	K_{srme} ↓	RMSD↓
GRACE-2L-OAM-L	26.4M	0.883	5.840	0.893	0.874	0.964	0.022	0.862	<u>0.169</u>	0.064
DPA3-3M-FT	3.27M	0.884	5.667	0.866	0.903	0.963	0.023	<u>0.869</u>	0.469	0.069
Nequip-OAM-L	9.6M	0.893	5.832	0.890	0.895	0.967	0.022	<u>0.865</u>	0.166	0.065
Allegro-OAM-L	9.7M	0.895	5.674	0.867	0.923	0.966	0.022	0.868	0.319	0.065
AlphaNet-v1-OMA	4.65M	0.901	5.747	0.879	0.924	0.968	0.024	0.831	0.644	0.079
SevenNet-MF-ompa	25.7M	0.901	5.825	0.890	0.911	0.969	0.021	0.867	0.317	0.064
ORB v3	25.5M	0.905	5.912	0.904	0.907	0.971	0.024	0.821	0.210	0.075
eqV2 M	86.6M	0.917	6.047	0.924	0.910	0.975	0.020	0.848	1.771	0.069
eSEN-30M-OAM	30.2M	0.925	6.069	0.928	0.923	0.977	0.018	0.866	0.170	<u>0.061</u>
MatRIS-10M-OAM	10.4M	<u>0.921</u>	<u>6.039</u>	<u>0.923</u>	<u>0.918</u>	<u>0.976</u>	<u>0.019</u>	0.871	0.218	0.060

Table 7: MatRIS performance on the non-compliant Matbench-Discovery benchmark with results on **10k most stable**.

Model	Param.	F1↑	DAF↑	Precision↑	Recall↑	Accuracy↑	MAE↓	R2↑	RMSD↓
GRACE-2L-OAM-L	26.4M	0.980	6.280	0.960	1.000	0.960	0.025	0.835	0.064
DPA3-3M-FT	3.27M	<u>0.987</u>	6.369	0.987	1.000	0.987	0.019	0.901	0.069
Nequip-OAM-L	9.6M	0.985	6.344	<u>0.985</u>	1.000	<u>0.985</u>	0.021	0.854	0.065
Allegro-OAM-L	9.7M	<u>0.987</u>	<u>6.371</u>	0.974	1.000	0.974	0.018	0.908	0.065
AlphaNet-v1-OMA	4.65M	0.965	6.312	0.980	1.000	0.980	0.020	0.882	0.079
SevenNet-MF-ompa	25.7M	0.970	6.346	0.985	1.000	<u>0.985</u>	0.019	0.888	0.064
ORB v3	25.5M	0.964	6.307	0.964	1.000	0.964	0.021	0.860	0.075
eqV2 M	86.6M	0.988	6.382	0.976	1.000	0.976	0.015	<u>0.904</u>	0.069
eSEN-30M-OAM	30.2M	0.971	6.350	0.971	1.000	0.971	<u>0.016</u>	0.901	<u>0.061</u>
MatRIS-10M-OAM	10.4M	0.986	6.366	0.973	1.000	0.973	0.015	<u>0.904</u>	0.060

We first performed the force field prediction task, in which the model is evaluated on datasets from the molecules, inorganic materials, and catalysis domains, predicting energies, forces, and virials. For fair comparison, we selected MLIPs trained on OMat+sAlex+MPTrj as reference. The results are reported in Table 8. Overall, MatRIS-10M-OAM achieves the best accuracy, and for molecules and inorganic materials, it generally outperforms other models in force prediction.

Table 8: Summary of model performance on LAMBench (Force Field Prediction). Energy (E) RMSE is in meV/atom, Force (F) RMSE in meV/Å, Virial (V) RMSE in meV/atom.

	GRACE-2L-OAM			SevenNet-MF-ompa			ORBv3-mpa			MatRIS-10M-OAM		
	E	F	V	E	F	V	E	F	V	E	F	V
Molecules												
AIMD-Chig (Wang et al., 2023)	3.1	239.8	-	3.4	247.9	-	2.4	<u>200.2</u>	-	<u>2.6</u>	200.0	-
ANI-1x (Smith et al., 2018)	32.1	365.5	-	26.1	337.7	-	20.0	<u>247.9</u>	-	<u>22.1</u>	246.1	-
MD22 (Chmiela et al., 2023)	3.5	235.9	-	4.7	238.1	-	<u>2.8</u>	<u>163.9</u>	-	2.4	161.5	-
Catalysis												
Vandermause et al. (2022)	5.5	<u>99.4</u>	60.6	12.7	100.8	39.1	6.8	92.6	51.2	13.8	110.9	<u>47.8</u>
Zhang et al. (2019)	251.6	723.0	-	<u>392.2</u>	<u>937.5</u>	-	464.9	1169.4	-	609.2	963.4	-
Fernández-Villanueva et al. (2024)	3.3	131.8	-	3.0	95.6	-	<u>2.0</u>	<u>86.4</u>	-	1.8	79.0	-
Inorganic materials												
Lopantsyna et al. (2023)	55.4	294.7	<u>200.1</u>	55.4	<u>268.8</u>	226.9	56.4	324.2	198.2	61.0	257.2	212.9
Lopantsyna et al. (2023)	<u>70.1</u>	309.7	243.1	69.8	<u>265.3</u>	235.8	71.0	330.6	<u>242.4</u>	75.6	261.2	251.6
Batzner et al. (2022)	0.8	111.5	-	0.7	107.9	-	0.6	<u>103.7</u>	-	0.6	103.4	-
Torres et al. (2019)	3.2	161.2	-	<u>2.8</u>	167.9	-	<u>2.8</u>	141.9	-	2.6	<u>148.5</u>	-
Gao et al. (2025)	17.8	135.7	164.1	<u>17.7</u>	<u>104.8</u>	161.1	20.4	167.4	141.4	14.9	83.9	<u>150.1</u>
Sours & Kulkarni (2023)	6.5	162.8	-	6.5	<u>173.6</u>	-	6.5	182.7	-	6.5	176.1	-

In addition, we also evaluated the performance on property calculation tasks, which include reaction barrier prediction (OC20-NEB task), elastic constant prediction (Elastic Properties task), and molecular conformer energy prediction (Wiggle150 task). The results are reported in Table 9. In the OC20-NEB task, MatRIS-10M-OAM achieves competitive results, but we observe that its pre-

dictions for reaction barriers (Ea) and reaction energies (d) are worse than those of other models, while its success rate remains relatively high. We speculate that this is because MatRIS uses MAE to compute energy loss during training, without placing extra weight on outlier data points, which amplifies their effect in this task; even so, the success rate is not significantly affected. In the elastic and Wiggle150 tasks, MatRIS-10M-OAM achieves the best performance.

Table 9: Summary of model performance on LAMBench (Property Calculation). Metrics are lower-is-better unless otherwise noted.

Model	OC20-NEB (Wander et al., 2025)					Elastic Properties		Wiggle150 (Brew et al., 2025)	
	MAE.Ea (eV)	MAE.d (eV)	Transfer (%) ↓	Desorption (%) ↓	Dissociation (%) ↓	Shear Modulus MAE (GPa)	Bulk Modulus MAE (GPa)	MAE (kcal/mol)	RMSE (kcal/mol)
GRACE-2L-OAM	1.6	0.7	65.1	<u>90.5</u>	72.2	9.1	<u>7.5</u>	12.1	14.0
SevenNet-MF-ompa	<u>2.1</u>	<u>1.3</u>	66.9	92.9	68.3	9.5	<u>7.5</u>	<u>11.0</u>	<u>12.8</u>
ORBv3-mpa	2.3	1.5	61.7	87.4	72.2	9.7	7.6	11.9	12.9
MatRIS-10M-OAM	4.0	3.6	<u>64.6</u>	90.6	<u>69.0</u>	8.8	6.4	9.5	10.6

Overall, the cross-domain evaluation on LAMBench shows that MatRIS-10M-OAM performs consistently well across both force field prediction and property calculation tasks, achieving either the best or highly competitive results, demonstrating strong generalizability and application potential.

D.3 ZEOLITE BENCHMARK

The Zeolite Dataset (Yin et al., 2025) comprises 16 zeolite structures relevant to catalysis, adsorption, and separation applications. For each type, atomic trajectories were generated via AIMD simulations at 2000 K using VASP. We adopt the pre-partitioned training, validation, and test sets, containing 48,000, 16,000, and 16,000 structures per zeolite, respectively. The model’s prediction targets are the total energies and atomic forces of the systems. The results are shown in Table 10; MatRIS achieves SOTA performance overall.

Table 10: MatRIS performance on Zeolite dataset. Energy(E) MAE is in **meV**, force(F) MAE is in **meV/Å**.

	Deep Pot		AlphaNet		DPA3-L24		MatRIS-M	
Type	E	F	E	F	E	F	E	F
ABWopt	90	90	<u>12</u>	<u>19</u>	13.7	19.1	3.4	6.8
BCTopt	110	50	<u>6.8</u>	<u>12</u>	<u>6.8</u>	<u>12.0</u>	3.0	4.9
BPHopt	210	60	<u>29</u>	16	28.6	<u>16.5</u>	39.2	8.3
CANopt	150	90	18	<u>15</u>	<u>17.3</u>	15.1	10.2	6.5
EDIopt	40	50	<u>8.7</u>	<u>13.5</u>	10.8	15.1	3.6	6.2
FERopt	290	130	43	28	41.6	<u>25.4</u>	30.6	11.9
GISopt	60	50	<u>11</u>	<u>11</u>	12.1	11.8	6.2	5.8
JBWopt	150	70	<u>10</u>	13	<u>9.7</u>	<u>12.4</u>	4.0	5.9
LOSopt	110	70	<u>21</u>	<u>12</u>	<u>21.0</u>	13.1	17.9	6.5
LTAopt	150	64	19	<u>12</u>	21.3	13.5	<u>20.5</u>	7.0
LTJopt	70	110	15	<u>11</u>	13.4	11.2	<u>14.4</u>	6.7
NATopt	210	110	<u>16</u>	<u>15</u>	17.2	15.6	8.0	7.4
PARopt	90	70	<u>18</u>	<u>24</u>	21.4	24.2	9.5	6.8
PHIopt	60	120	<u>20</u>	<u>14</u>	<u>19.6</u>	14.4	15.9	7.5
SODOpt	200	110	<u>9.5</u>	<u>12</u>	11.0	13.4	4.4	5.7
THOopt	160	60	<u>17</u>	<u>15</u>	20.2	16.9	7.5	8.0

D.4 DPA2 TEST SET

We evaluate the performance of the MatRIS model on the DPA2 dataset (Zhang et al., 2024) to assess its ability to handle small-scale datasets. This composite dataset integrates 18 domain-specific subsets (e.g., Alloy, Drug, H₂O, OC2M) and is generated using various DFT software packages (e.g.,

Table 11: MatRIS performance on DPA2 test sets from Zhang et al. (2024). Energy (**E**) RMSE is in **meV/atom**, force (**F**) RMSE is in **meV/Å**. ‘OOM’ indicates an Out-Of-Memory error. ‘NC’ indicates that the model employs a non-conservative force prediction.

		GemNet-OC ^{NC}		NequIP		MACE		eqV2 ^{NC}		DPA3-L24		MatRIS-M	
Dataset	Size	E	F	E	F	E	F	E	F	E	F	E	F
Alloy	71K	14.3	<u>85.1</u>	44.0	175.6	16.2	190.2	8.5	62.7	<u>7.1</u>	99.2	5.8	96.2
Cathode-P	59K	1.5	17.9	14.3	69.8	2.6	37.8	1.1	<u>14.9</u>	<u>0.6</u>	18.6	0.3	11.9
Cluster-P	139K	47.7	69.6	75.1	216.6	41.3	189.7	34.6	<u>104.4</u>	<u>29.3</u>	118.3	12.8	113.9
Drug	1380K	40.5	93.6	21.6	187.2	-	-	29.8	807.4	<u>5.5</u>	<u>54.2</u>	1.4	39.7
FerroEle-P	7K	1.5	17.9	1.1	23.0	2.3	31.7	1.1	<u>13.0</u>	<u>0.3</u>	13.4	0.2	10.9
OC2M	2000K	25.0	129.1	97.4	226.1	-	-	<u>6.7</u>	45.2	9.0	128.0	5.9	<u>77.9</u>
SSE-PBE-P	15K	2.7	8.2	1.6	41.1	1.8	29.9	OOM	OOM	<u>0.5</u>	<u>19.8</u>	0.3	11.4
SemiCond	137K	8.0	<u>94.4</u>	20.5	180.7	12.7	182.8	3.9	40.8	<u>3.4</u>	108.3	2.7	95.0
H2O-PD	46K	OOM	OOM	0.9	27.1	79.9	29.7	OOM	OOM	<u>0.4</u>	<u>13.7</u>	0.3	10.7
AgUAu-PBE	17K	106.0	<u>8.0</u>	42.3	43.8	369.1	34.5	23.4	4.4	1.1	10.9	<u>2.5</u>	10.7
AlUMgUCu	24K	5.9	<u>9.4</u>	38.0	48.3	7.7	42.9	<u>1.9</u>	5.7	2.0	13.0	1.2	15.9
Cu	15K	6.1	<u>5.8</u>	6.2	16.7	38.8	13.6	<u>1.7</u>	3.8	<u>1.7</u>	7.2	0.5	6.1
Sn	6K	8.4	<u>33.7</u>	18.2	62.2	-	-	5.2	19.6	<u>2.9</u>	49.8	2.3	45.9
Ti	10K	44.5	87.9	27.6	137.4	8.3	94.2	19.1	48.6	<u>4.1</u>	91.7	3.3	<u>80.2</u>
V	15K	17.9	79.3	8.8	91.6	14.2	140.4	5.6	47.4	<u>2.8</u>	71.8	1.9	<u>62.9</u>
W	42K	79.1	81.2	20.8	160.4	15.6	181.2	46.8	51.3	<u>2.5</u>	83.3	1.9	<u>66.3</u>
C12H26	34K	125.8	<u>518.7</u>	121.4	715.6	81.9	802.3	123.1	907.4	<u>42.4</u>	541.6	19.5	287.6
HfO2	28K	1.2	16.1	1.5	58.8	2.3	14.7	<u>1.0</u>	9.1	1.4	28.9	0.3	<u>14.6</u>

VASP, Gaussian, ABACUS), with the training data for each subset ranging from 6K to 2,000K. We evaluate MatRIS-M using the same training configurations and maintain consistency with the training and test sets as in Zhang et al. (2024) to ensure comparability. More detailed hyper-parameters are reported in Table 12.

All results are summarized in Table 11, with benchmark data for other models taken from Zhang et al. (2024; 2025). Overall, MatRIS-M achieves better accuracy in both energy and force predictions, demonstrating its robustness across diverse domains. Notably, however, eqV2 and GemNet-OC exhibit lower force errors than MatRIS in certain systems. This advantage likely stems from their non-conservative force prediction, where energy and forces are fitted separately at the expense of physical consistency.

D.5 MD STABILITY EVALUATION

We assessed the stability of MatRIS by examining energy conservation in MD simulations under the NVE ensemble (microcanonical ensemble), using energy drift and thermostatted stability as evaluation metrics. The test data were taken from LAMBench (Peng et al., 2026), including organic molecules and inorganic material systems, which are out-of-distribution for MatRIS-M trained on MPTrj dataset. For each system, atomic velocities were first randomly initialized at 300 K using the Maxwell-Boltzmann distribution. Subsequently, MD simulations were performed in the NVE ensemble for 80 ps with a 1 fs time step.

Figure 9 shows the results of the MD simulations. MatRIS-M is able to conserve energy over long simulations, with both the total energy and the kinetic temperature fluctuating around their initial values, and no large drifts are observed.

E TRAINING DETAILS AND HYPER-PARAMETERS

We summarize the hyperparameters of the models across different datasets and versions in Table 12. For the MPTrj dataset, we experimented with models of different sizes by varying the number of layers (S, M, and L correspond to 4, 6, and 10 layers, respectively). The learning rate follows a cosine annealing schedule, decaying to the minimum value at the last epoch. In distributed training,

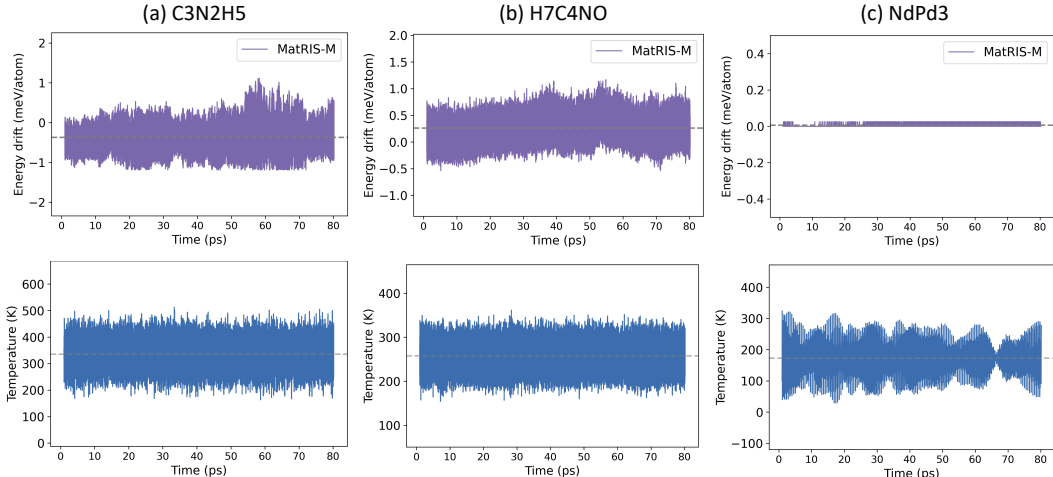


Figure 9: NVE MD simulations of three systems using MatRIS-M. The top row shows the energy drift, and the bottom row shows the time series for the kinetic temperature.

we implemented a load balancing scheme to reduce synchronization overhead (see Section C.1), so the number of samples per GPU may vary; the table reports the average global batch size. Notably, the loss reduction in distributed training is performed using a graph-level scheme to avoid bias toward larger systems (see Section C.2). Additionally, for the Matbench-Discovery benchmark, we pre-trained the MatRIS-M and L models with a denoising process to enhance generalization, with details in Section C.3.

Table 12: Hyper-parameters for MatRIS variants reported in this paper. In MatRIS-OAM, values outside parentheses denote the OMat configuration, those in parentheses the sAlex+MPTrj fine-tuning configuration, and values without parentheses are shared.

Hyper-parameters	MPTrj-S	MPTrj-M	MPTrj-L	MatRIS-OAM	SPICE-M	MatPES-1.4M	Others
Number of MatRIS layers	4	6	10	10	6	3	6
Dimension of atom features	128	128	128	128	128	64	128
Dimension of edge features	128	128	128	128	128	64	128
Dimension of three-body features	128	128	128	128	128	64	128
Radial basis function	Bessel	Bessel	Bessel	Bessel	Bessel	Bessel	Bessel
Number of radial basis functions	7	7	7	7	7	7	7
Pairwise cutoff	6.0	6.0	6.0	6.0	6.0	6.0	6.0
Three-body cutoff	4.0	4.5	4.5	4.5	4.0	4.0	4.0
Global batch size (avg)	512	512	320	512(320)	128	64	1/256
Optimizer	AdamW	AdamW	AdamW	AdamW	AdamW	Adam	AdamW
Weight decay	1e-2	1e-2	1e-2	1e-3	1e-3	0.0	1e-3
Maximum Learning rate	5e-4	3e-4	3e-4	3e-4(1e-4)	3e-4	3e-4	3e-4
Minimum Learning rate	5e-6	3e-6	3e-6	3e-6(1e-6)	3e-6	3e-6	3e-6
Learning rate scheduling	CosLR	CosLR	CosLR	CosLR	CosLR	CosLR	CosLR
Number of epochs	30	40	100	4(8)	200	30	100
Loss function	Huber($\delta=0.01$)	Huber($\delta=0.01$)	MAE / L2MAE	MAE / L2MAE	Huber($\delta=0.01$)	MAE	Huber($\delta=0.01$)
Gradient clipping norm	0.5	0.5	0.5	0.5	0.5	0.5	0.5
Energy loss prefactor	5	5	5	5	5	5	5
Force loss prefactor	5	5	5	5	5	5	5
Stress loss prefactor	0.1	0.1	0.1	0.1	-	0.1	0.1
Magmom loss prefactor	0.1	0.1	0.1	0.1	-	0.1	-
Denoising Settings							
Corruption probability	-	100%	100%	-	-	-	-
Maximum number of steps	-	1000	1000	-	-	-	-
Maximum sigma	-	1.0	1.0	-	-	-	-
Minimum sigma	-	0.0	0.0	-	-	-	-
Noise Schedule	-	Linear	Linear	-	-	-	-
Number of epochs	-	20	20	-	-	-	-